https://doi.org/10.5194/egusphere-2025-5551
Preprint. Discussion started: 5 December 2025

Constraining Rain Evaporation from Shallow-Clouds in the Trades using an Observation-Based Superdroplet Model

Nils Niebaum[1,*], Clara J.A. Bayley[2,3,*], Florian Poydenot[1], Ann Kristin Naumann[1,2,4], Mampi Sarkar[5,6], and Raphaela Vogel[1]

[1]Meteorologisches Institut, Universität Hamburg, Hamburg, Germany
[2]Max-Planck-Institut für Meteorologie, Hamburg, Germany
[3]International Max Planck Research School on Earth System Modelling, Hamburg, Germany
[4]Ludwig-Maximilians-Universität München, Munich, Germany
[5]Institute of Climate and Atmospheric Science, University of Houston, Houston, TX, USA
[6]Department of Earth and Atmospheric Sciences, University of Houston, Houston, TX, USA
[*]These authors contributed equally to this work.

Correspondence: Clara J.A. Bayley (clara.bayley@mpimet.mpg.de)

Abstract. Rain evaporation influences subcloud moisture and energy budgets as well as boundary layer buoyancy, making it important for shallow cumulus organization. This study constrains the amount of, and controls on, rain evaporation in the subcloud layer of trade-wind shallow cumuli. We combine observations from the EUREC^{4}A field campaign with a 1D rainshaft using superdroplet model (SDM) microphysics. With SDM we explicitly resolve how the observed droplet size distributions (DSDs) evolve beneath cloud-base, and explore, for the first time, the potential impact of raindrop collisions. Constraining the amount of evaporation, we find mean column integrated evaporative cooling of $150 \pm 170\ \mathrm{W\ m^{-2}}$, and evaporation fraction of $30 \pm 20\%$. The dominant controls on rain evaporation are the subcloud relative humidity and the cloud-base DSD. Subcloud relative humidity determines the slope of the evaporation profiles, and cloud-base rain water content (RWC) controls the column integrated cooling. In contrast, evaporation fraction can vary substantially between clouds, even with comparable RWC, because of small differences to the cloud-base DSD. For narrow DSDs, the evaporation fraction is well captured by an analytical approximation, which also highlights the importance of ventilation effects on evaporation. We find collisions have negligible impact on rain evaporation, however, beyond rain rates of $\approx 3\ \mathrm{mm\ h^{-1}}$, differences emerge which suggest that collisions, in particular those causing severe droplet breakup, need to be considered for heavier precipitation. Our results stress the importance of accurately measuring and modeling DSDs for rain evaporation, but justify the use of simpler microphysics models that only represent condensation/evaporation for lightly precipitating regimes as observed during EUREC^{4}A.

1 Introduction

Below every precipitating cloud, raindrops pass through unsaturated air on their way towards the surface and evaporate either partially or completely. This sub-cloud layer rain evaporation reduces precipitation efficiency and therefore the amount of rain that reaches the surface (Seifert and Heus, 2013; Naumann and Seifert, 2016; Narenpitak et al., 2021; Sarkar et al., 2023; Radtke et al., 2023). Rain evaporation also moistens and cools the surrounding air, thereby influencing the energetics and stability of the

https://doi.org/10.5194/egusphere-2025-5551
Preprint. Discussion started: 5 December 2025

atmosphere. But above all, rain evaporation is a key component of the cloud life cycle. The cooling effect from rain evaporation makes air negatively buoyant, driving downdrafts which spread radially outward when reaching the surface in the form of cold-pools (e.g. Zuidema et al., 2012; Rochetin et al., 2021). These cold pools go on to trigger a chain of dynamic processes that influence the mesoscale organization and amount of clouds (Zuidema et al., 2017; Vogel et al., 2021; Alinaghi et al., 2025). In the trade-wind regions, precipitating cumuli are frequent and, due to the relative dryness of the trades, rain evaporates efficiently and triggers cold pools frequently (Nuijens et al., 2009; Vogel et al., 2021). Overall, cold pools occur about 7.8% of the time during a day and about 73% when averaged over all days in the winter trades (Vogel et al., 2021; Touzé-Peiffer et al., 2022). Cold pools thus have a strong impact on both the coverage and organization of trade cumuli, with consequences for cloud radiative feedbacks and precipitation patterns (Zuidema et al., 2017; Schulz et al., 2021; Vogel et al., 2021; Radtke et al., 2022, 2023; Alinaghi et al., 2025). Rain evaporation therefore has a critical impact on the energetics, structure, and cloudiness of the trade-wind boundary layer. However, its magnitude and controls have not yet been constrained.

Due to a shortage of field observations, it is difficult to robustly quantify rain evaporation rates from direct measurements. Tridon et al. (2017) developed a method to obtain droplet size distributions (DSDs) from Doppler velocity spectra measured with K_a and W band Doppler radars. They retrieved evaporative cooling rates from a continental deep convection system in the sub-cloud layer between $0.75 - 3\ \mathrm{km}$ above sea level, with a large range up to $60\ \mathrm{K\ d^{-1}}$ (or equivalently roughly $422\ \mathrm{W\ m^{-2}}$). Their retrieved vertical profiles indicate most evaporation in the middle of the sub-cloud layer. However there are large uncertainties in the retrieval method of Tridon et al. (2017), and, because deep continental convection differs strongly from winter trades, direct analogies are limited. Disentangling the various factors influencing rain evaporation using field observations remains even more elusive.

Models for rain evaporation are also scarce, and so far limited to models of condensation/evaporation using bin microphysics schemes. Sarkar et al. (2023) used DSDs from in-situ cloud probes during the EUREC^{4}A/ATOMIC campaign (Leandro and Chuang, 2021; Pincus et al., 2021) to simulate trade-wind rain evaporation with a 1-D rainshaft model with bin scheme microphysics. They found 63% of the rain mass to evaporate in the sub-cloud layer in the mean, and a spread in latent cooling of $15 - 352\ \mathrm{W\ m^{-2}}$. Unlike Tridon et al. (2017), their evaporation profiles showed stronger evaporation near the cloud-base (top-heavy) than near the surface (bottom-heavy) for the majority of profiles. Sarkar et al. (2023) were able to show the measured rain water content (RWC) was a dominant constraint on the column integrated evaporation rate. They also identified that the shape and mean radius of the DSD controls the top- vs. bottom-heaviness, with larger raindrops favouring bottom-heaviness. The large inter-cloud spread of evaporation simulated by Sarkar et al. (2023) highlight the challenge in constraining the magnitude, variability and vertical structure of rain evaporation, for which we need both more observations and modeling.

An alternative and arguably more realistic way to model rain evaporation is through Superdroplet Models for cloud microphysics (SDMs; Shima et al., 2009; Sölch and Kärcher, 2010; Andrejczuk et al., 2010; Riechelmann et al., 2012; Hoffmann et al., 2015; Arabas et al., 2015; Naumann and Seifert, 2015; Brdar and Seifert, 2018; Bartman et al., 2022; Bayley et al., 2025a). SDM is a Lagrangian particle model which represents a group of similar droplets with comparable radius, velocity, and mass of solute through one simulated particle called a superdroplet. The multiplicity of a superdroplet accounts for the number of real droplets

https://doi.org/10.5194/egusphere-2025-5551
Preprint. Discussion started: 5 December 2025

it represents, and all microphysical processes are modeled explicitly (i.e. each superdroplet evolves freely and individually), except for collisions between droplets which are modeled probabilistically (Shima et al., 2009; Bayley et al., 2025b).

In contrast to classical bin and bulk schemes, SDM has numerous conceptual and computational advantages (Grabowski et al., 2018; Morrison et al., 2020). Relevant for this study, are that SDM does not suffer from numerical diffusion, it makes no assumptions about droplet categories nor size distributions, and it models condensation/evaporation according to fundamental Köhler theory (Köhler, 1936; Pruppacher and Klett, 2010). The strong relationship between SDM and our fundamental theoretical understanding of cloud microphysics makes SDM a highly suitable model for studying the magnitude and controls on rain evaporation.

By using a SDM, we are also able to investigate the indirect effect of droplet collisions on rain evaporation. Previous studies using bin scheme microphysics neglected the effect of collisions between droplets on rain evaporation (Sarkar et al., 2023, 2025). However, whilst collisions between droplets do not change the total mass of raindrops, they do change the distribution of mass across raindrop sizes, and therefore could impact the total rate of evaporation. Collisions leading to droplet coalescence shift mass towards larger droplets, which fall faster and have a smaller surface to volume ratio than smaller droplets, therefore lowering the evaporation rate (Hu and Srivastava, 1995; Seifert, 2008). Conversely, collisional breakup shifts mass towards smaller, faster-evaporating droplets, and the higher the number of fragments, the stronger this effect. Rebound has no effect except that it makes coalescence less likely than if it did not occur. The net effect of collisions (coalescence, rebound, and breakup) on sub-cloud rain evaporation has not been assessed before, but nevertheless may be significant.

Taking into account the advantages of SDM and our ability to model droplet collisions with it, this study uses SDM to quantify rain evaporation beneath trade-wind shallow-cumuli, as well as elucidate how the evaporation is impacted by microphysical processes, ambient thermodynamic conditions (including cloud-base height), and the DSD. We setup the SDM called CLEO (Clouds through Lagrangian Exascale micrO-physics; Bayley et al., 2025a; Bayley, 2025) to model steady-state 1-D rainshafts for clouds with cloud-base DSDs and thermodynamic profiles fitted from the EUREC^{4}A campaign. To our knowledge this is the first time SDM has been applied to quantify sub-cloud rain evaporation in the trades, also constrained by field observations, and accounting for the effect of droplet collisions.

The paper is structured as follows: Section 2 describes how we used the observational data and the setup of our rainshaft model; Section 3 presents the influence we have found of ambient thermodynamics, the cloud-base DSD, and microphysical processes on rain evaporation; Section 4 summarizes our findings and gives an outlook.

2 Data and Methods

2.1 Observational Data

To model realistic conditions representative of the sub-cloud layer beneath shallow trade-wind cumuli, we use observational datasets for the cloud-base DSDs and thermodynamic conditions from the EUREC^{4}A campaign (ElUcidating the RolE of Clouds-Circulation Coupling in ClimAte) as the basis for our rainshaft. EUREC^{4}A took place in the tropical North Atlantic upstream of Barbados from January 20th to February 20th 2020 to understand and quantify the interaction of trade cumulus clouds with their

https://doi.org/10.5194/egusphere-2025-5551
Preprint. Discussion started: 5 December 2025

atmospheric and oceanographic environment across a range of scales, from micro- to meso-scale (Bony et al., 2018; Stevens et al., 2021).

For the cloud-base DSDs, we use in-situ measurements at $1\ \mathrm{Hz}$ resolution, corresponding to approximately $100\ \mathrm{m}$ spacing between measurements. We use the pre-merged product by Coutris (2021) based on the CDP-2 and 2DS instruments onboard the ATR aircraft (Bony et al., 2022). The measurements cover droplet radii from $1\ \mu\mathrm{m}$ to $1.275\ \mathrm{mm}$ in non-uniform radii bins (Coutris, 2021; Bony et al., 2022). From this dataset, we identify individual "rain clouds" from 19 cloud-base rectangular flight tracks between $500 - 1200\ \mathrm{m}$ altitude flown east of Barbados over 11 days following the definition from Bony et al. (2022) that rain measurements contain raindrops of at least $250\ \mu\mathrm{m}$ radius. We then define an individual cloud as at least three consecutive rain measurements, which gives all clouds a horizontal extent of at least $300\ \mathrm{m}$, given the ATRs flight speed of approximately $100\ \mathrm{m\ s^{-1}}$. Because the concentration of raindrops is very low compared to the measurement volume of the devices ($30\ \mathrm{cm^3}$), we allow for up to five consecutive rain-free measurements in-between individual rain measurements to still count as one rain cloud.

To facilitate comparability to other studies we fit the cloud-base DSD measurements for each rain cloud with a bimodal log-normal distribution. Although this is not a necessary requirement for SDM, by fitting an analytic form to the cloud-base DSDs, bulk and bin schemes, which necessarily or often make similar approximations, can also use our droplet initialization data (e.g. Seifert, 2008; Sarkar et al., 2023). The bimodal log-normal DSD of each cloud is the sum of two log-normal probability distributions, $L(r)$, for droplets of radius r following Equation 1, where N_a is the total number of drops, μ_g is the geometric mean radius of the distribution (i.e. the median of the distribution), and σ_g is the geometric standard deviation of the distribution.

$$L(r) = \frac{N_a}{\sqrt{2\pi}\, r \ln \sigma_g} \exp\left(-\frac{(\ln r - \ln \mu_g)^2}{2(\ln \sigma_g)^2}\right) \quad \text{for } r > 0 \tag{1}$$

We further choose to fit the bimodal distributions only for radii greater than $50\ \mu\mathrm{m}$, which represents the boundary to cloud droplets (Bony et al., 2022; , AMS); thereby avoiding modeling droplets which do not fall at an appreciable speed and therefore are not relevant to the rainshaft. Our fitting algorithm also weights individual radii bins of the observational data based on the cube of the radius, giving greater weight to larger radii bins in the loss function. These would otherwise be underrepresented compared to the highly numerous small droplets, although they contain most of the RWC. As a final constraint on the modeled DSDs, we remove 13 outliers whose fitted distributions do not agree with the observed RWC (Section 2.3).

For most clouds, the fitted bimodal log-normal distribution is well in line with the temporal mean of the observations. Figure 1c shows the fitted DSD overlain on the measured droplet sizes for a typical cloud. The fitted cloud RWC in our model also aligns closely with the observed temporal mean RWC for each cloud, as shown by Figure 1d, with a Pearson correlation coefficient $R = 0.99$ (log-log Pearson correlation coefficient of $R_{\log} = 0.91$).

We use the JOANNE dropsonde dataset Level 3 Version 2.0.0 (George et al., 2021; George, 2021) to get humidity and temperature profiles in the vicinity of the measured DSDs for each cloud. First we identify the dropsondes released by HALO and P3 within $100\ \mathrm{km}$ and within $\pm 3\ \mathrm{h}$ of the DSD measurements made for each cloud. This definition is contentious, since the clouds whose DSDs we measure have much smaller time- and length-scales, but it allows for a more representative sample of the dropsonde measurements. After identifying corresponding dropsondes for individual clouds, we fit the thermodynamic profiles for each

https://doi.org/10.5194/egusphere-2025-5551
Preprint. Discussion started: 5 December 2025

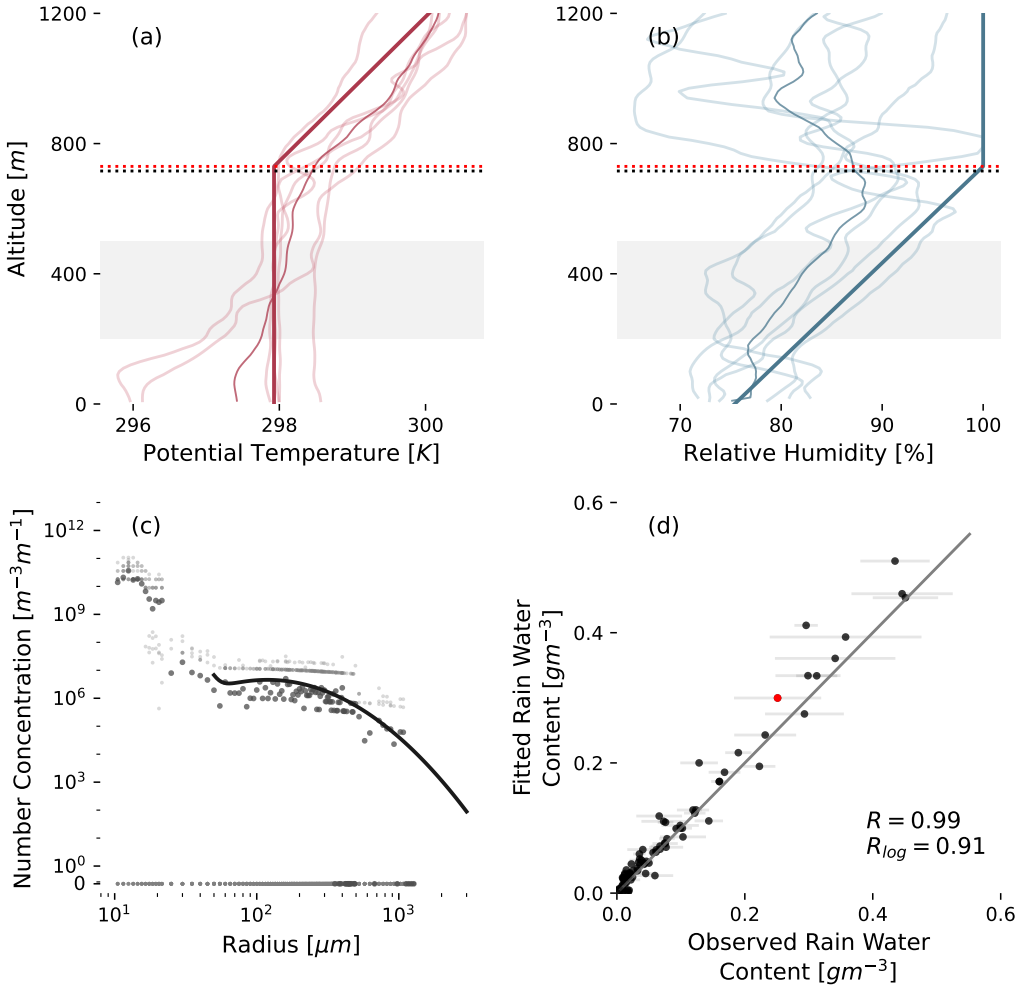

Figure 1. Example of DSD and thermodynamic fits for a randomly selected cloud (a,b,c), typical of the entire cloud population we simulate . (a, b) The thermodynamic fits (thick dark line) overlaid on the 6 individual dropsonde measurements (thin light line) and their mean (thin dark line); (a) shows potential temperature (red); (b) shows relative humidity (blue). Data within the grey shaded altitude range from $200 - 500$ m was used for the linear fits. The horizontal dashed black lines denote the flight altitude of the ATR aircraft, and the dashed red lines denote the altitude of 100% relative humidity given by the fit in panel (b). (c) The applied bimodal fit (solid black line) overlaid on the 23 s of ATR measurements of the number concentration of droplets in each radius bin (small light grey dots) and their temporal mean (large dark grey dots). Note that the y-axis changes from logarithmic to linear scale below 10^{-1} to show 0 values. (d) Comparison of the RWC of the fitted DSDs for each cloud used by the rainshaft model against the RWC from the observational cloud composite dataset as black dots. The error bars denote the standard error of the mean of the observations. The red dot indicates the example cloud used for panel (a,b,c).

https://doi.org/10.5194/egusphere-2025-5551
Preprint. Discussion started: 5 December 2025

cloud with a constant potential temperature, a linear relative humidity, and a linear pressure profile. For the potential temperature and pressure profiles, we fit to the dropsonde measurements between $200 - 500$ m. For the relative humidity profile, we also fit to the dropsonde measurements between $200 - 500$ m but give dropsondes with moister profiles between $100 - 700$ m more weight (using a smoothed weight with constant prior). We do so, because moister profiles are more likely to represent atmospheric conditions below clouds than the clear-sky regions. Finally, cloud-base is defined as the altitude of 100% relative humidity. An example for the thermodynamic fits can be seen in Figure 1a,b,c. Figure 1b further indicates that our fit follows the moister profiles more closely, and that the cloud-base altitude at 100% relative humidity aligns well with the ATR flight altitude.

The resulting dataset excluding outliers contains 102 precipitating trade-wind shallow-cumuli clouds, each with their own fitted thermodynamic profiles and DSDs.

2.2 Setup of the Superdroplet Model CLEO

We use the Superdroplet Model CLEO, version `v0.39.7`, to simulate all the relevant warm-cloud microphysical processes for our study (Bayley et al., 2025b; Bayley, 2025). We run CLEO as a quasi-stationary 1-D rainshaft to represent each cloud in our sample of identified rain clouds from the EUREC^{4}A observations (Section 2.1). This means we keep the thermodynamic profiles and the cloud-base DSD constant in time, matched to the observations, and examine the time-averaged statistics of the sub-cloud layer once it reaches a quasi-stationary state (Section 2.3). In this way we obtain a "snapshot" of each cloud's precipitation flux, evaporation rate and evaporation fraction, but do not explore the time-evolution of the cloud, in which heavy rain may influence its environment e.g. through turbulent mixing, downdrafts, and aerosol depletion.

For each cloud in our sample, we divide the 1-D rainshaft into a cloud-base and a sub-cloud layer. The cloud-base is a single layer 100 m thick with constant thermodynamics, and where the fitted DSD is applied by randomly sampling it at every motion time-step (2 s). To randomly sample the DSD, we randomly draw a superdroplet from each of 2048 uniformly-spaced logarithmic bins between 50 μm to 3 mm and assign its multiplicity according to the fitted DSD. At the end of each timestep we remove any remaining superdroplets from the cloud-base layer and initialize 2048 new superdroplets. Superdroplets which fall into the (initially empty) sub-cloud layer are not removed and thereafter evolve freely. The sub-cloud layer has a 20 m grid-spacing and the total height of each column varies with the fitted cloud-base height. Within the quasi-stationary state each gridbox contains roughly 128 activated superdroplets, which is deemed sufficient for convergence of the SDM collision algorithm, given we average over the quasi-stationary state (equivalent to approximately 1000 separate SDM realizations) (Unterstrasser et al., 2017; Morrison et al., 2020; Unterstrasser et al., 2020; Morrison et al., 2024).

We use four microphysical setups to investigate the importance of droplet collisions, and these are summarized in Table 1. All the setups simulate droplet motion (droplets falling according to their terminal velocity) and evaporation/condensation. The EvapOnly setup models no additional processes and is considered as the "control" scenario because it is most comparable to previous studies which also quantified rain evaporation (Tridon et al., 2017; Sarkar et al., 2023, 2025). The EvapCoal setup additionally simulates collision-coalescence to examine the effect of collisions between droplets in the absence of collisional breakup and rebound, as is typically assumed by conventional microphysics models. The EvapCoalBuRe-many and EvapCoalBuRe-few setups further include collisional rebound and breakup as well as coalescence and they differ in the frag-

https://doi.org/10.5194/egusphere-2025-5551
Preprint. Discussion started: 5 December 2025

ments they produce when breakup occurs. Due to the large uncertainty in parameterizing fragments from collisional breakup, we choose to prescribe a fixed number of fragments per breakup event: EvapCoalBuRe-few produces 5, whereas EvapCoalBuRe-many produces 50. EvapCoalBuRe-few (5 fragments) represents the lower bound and EvapCoalBuRe-many (50 fragments) represents the upper bound on evaporation enhancement by breakup. This bracketing strategy bounds sensitivity of evaporation to breakup while ensuring that our results are not tied to a single uncertain parameterization.

	Terminal velocity	Evaporation/Condensation	Collisional Coalescence	Collisional Coalescence, Breakup & Rebound
Parameterisation	R1993; (see also B2025b)	explicit Köhler theory as in B2025b	L1974 hydrodynamic kernel as formulated by S2002	L1974 hydrodynamic kernel with coalescence/breakup/rebound efficiencies from Sch2010, Str2010; (see also B2025b)
EvapOnly	Yes	Yes	No	No
EvapCoal	Yes	Yes	Yes	No
EvapCoalBuRe-few	Yes	Yes	Yes	Yes (5)
EvapCoalBuRe-many	Yes	Yes	Yes	Yes (50)

Table 1. Model setups used in this study and the parameterisations for each microphysical process. For collisional breakup, we prescribe a fixed number of fragments produced per breakup event, given in brackets. Acronyms in the table: R1993 = Rogers et al. (1993), B2025b = Bayley et al. (2025b), L1974 = Long (1974), S2002 = Simmel et al. (2002), Sch2010 = Schlottke et al. (2010), and Str2010 = Straub et al. (2010).

CLEO outputs evaporation rates directly from the Köhler theory ODE for the change in radii of the droplets via evaporation/-condensation (Bayley et al., 2025b). The column integrated evaporation mass flux, $F_{e,\mathrm{tot}}$, is then the sum of the evaporation rate across all gridboxes, and the evaporation fraction (ξ) is given as the fraction of quasi-stationary mean integrated evaporation flux and the quasi-stationary mean cloud-base precipitation flux ($F_{p,\mathrm{cb}}$), thus $\xi = \langle F_{e,\mathrm{tot}} \rangle / \langle F_{p,\mathrm{cb}} \rangle$ (Section 2.3).

In the following sections, the mean mass radius, $\overline{r_{\mathrm{M}}}$, is the mean of the mass weighted distribution of droplet radii. It is calculated as $\overline{r_{\mathrm{M}}} = \sum_i \frac{r_i \cdot m_i}{M}$, where r_i and m_i are the radius and mass of an individual raindrop ($i \in [0, N]$) and M is the total mass of all raindrops, $M = \sum_i m_i$.

2.3 Validation of model setup

Quasi-stationary state: The spin-up phase, when droplets initially start falling into the sub-cloud layer and precipitation increases, lasts about 300 s (Figure 2). After the spin-up, all clouds show stable precipitation and the model is in a quasi-stationary state with variance induced by our random sampling of superdroplets. We analyse the mean over the quasi-stationary state from

https://doi.org/10.5194/egusphere-2025-5551
Preprint. Discussion started: 5 December 2025

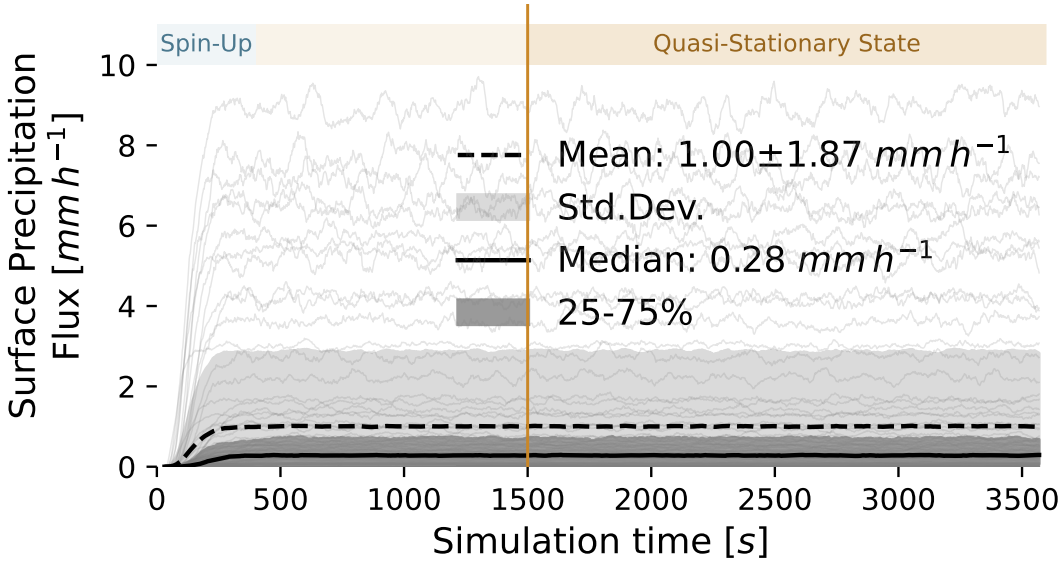

Figure 2. Temporal evolution of surface precipitation in the EvapOnly setup against simulation time. Individual clouds are shown as thin, grey lines with a rolling mean over 60 s. The mean over all clouds is shown as a dashed thick black line with the corresponding standard deviation in light grey shading. The median over the clouds as solid thick black line, with the inter-quartile-range as dark grey shading. Colored horizontal bars at the top roughly indicate the spin-up phase in blue and quasi-stationary state in orange. We use data past 1500 s (vertical orange line) as quasi-stationary state for our analysis. Temporal mean values over the quasi-stationary state are shown in the legend.

1500 s until the end of the simulation at 3600 s, thereby ensuring that even the slowest falling droplets have penetrated into the surface layers, and so the DSD at each height is in dynamic equilibrium. In this way we obtain our "snapshots" of each cloud's precipitation flux, evaporation rate and evaporation fraction.

Outliers: We omit all clouds which exceed the inter-cloud mean surface precipitation and column integrated evaporation rate by more than 4 standard deviations. In other words, we omit 1.7% of the clouds, those that have cloud-base precipitation exceeding $23.18\ \mathrm{mm\ h^{-1}}$ and column integrated evaporation of $2.37\ \mathrm{mm\ h^{-1}}$. We further exclude 13 clouds for which the fitted DSD's RWC is not within $66 - 150\%$ of the observed RWC. In total, we analyze 102 clouds.

Precipitation and RWC: Figure 3 shows the distributions of cloud RWC and surface precipitation flux for the quasi-stationary state of all the clouds in the EvapOnly simulations. The distribution of surface precipitation flux covers a range from $0 - 10\ \mathrm{mm\ h^{-1}}$ with a strong skew towards lower values, a mean of $1.00 \pm 1.89\ \mathrm{mm\ h^{-1}}$ and a median of $0.28\ \mathrm{mm\ h^{-1}}$. This spread is also aligned with observations, such as those taken aboard of *MS Merian* during the EUREC^{4}A campaign, which measured mean surface rain rates ranging from $0 - 7.43\ \mathrm{mm\ h^{-1}}$ (Acquistapace et al., 2022). In addition, our values span a range which includes both the climatological mean rain rates and rain intensity of trade wind cold pools identified by Vogel et al. (2021) at the Barbados Cloud Observatory.

https://doi.org/10.5194/egusphere-2025-5551
Preprint. Discussion started: 5 December 2025

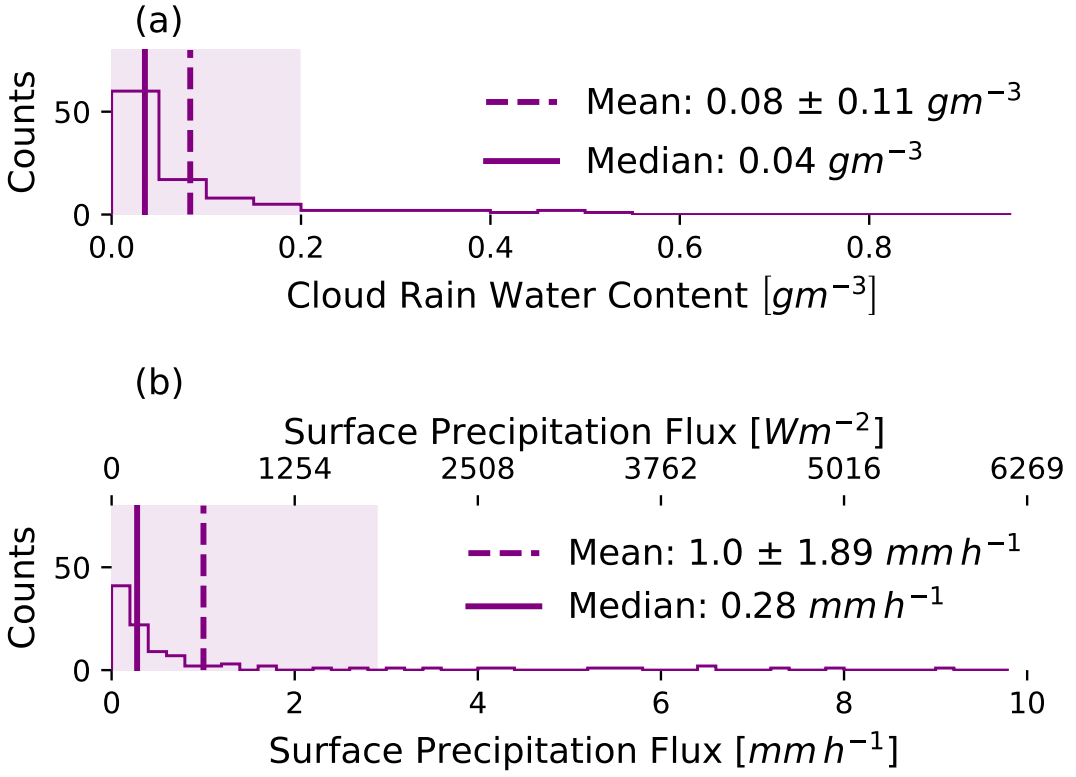

Figure 3. Histograms of (a) cloud RWC and (b) surface precipitation flux for the EvapOnly setup. Mean denoted as dashed vertical line with standard deviation as shading. Median as solid vertical line. Values are shown in the legend.

3 Results and Discussion

First of all, we quantify the sub-cloud evaporation for our sample of 102 clouds simulated with the "control", EvapOnly setup. Figure 4 shows the distributions of column integrated evaporative cooling and evaporation fraction and both distributions are skewed towards lower values: the evaporative cooling ranges from $0 - 800$ W m^{-2} with a mean of 150 ± 170 W m^{-2} and a median of 72 W m^{-2}. The evaporation fraction ranges from $0 - 80\%$ and is less skewed, with a mean of $30 \pm 20\%$ and a median of 25.6%. Somewhat surprisingly, the column integrated evaporative cooling and the evaporation fraction are independent quantities, with a correlation $R = 0.00$ (Figure A1a).

The vertical evaporation profile is remarkably similar for almost all the clouds, with more evaporation near the surface (bottom-heavy). Figure 5 shows the vertical profile of evaporative cooling with altitude, normalized to the individual cloud-base height for each cloud. Whilst there is considerable spread in the evaporation rates, except for a few rare cases, the maximum evaporation rate occurs in the lowest third of the rainshaft for all the clouds.

https://doi.org/10.5194/egusphere-2025-5551
Preprint. Discussion started: 5 December 2025

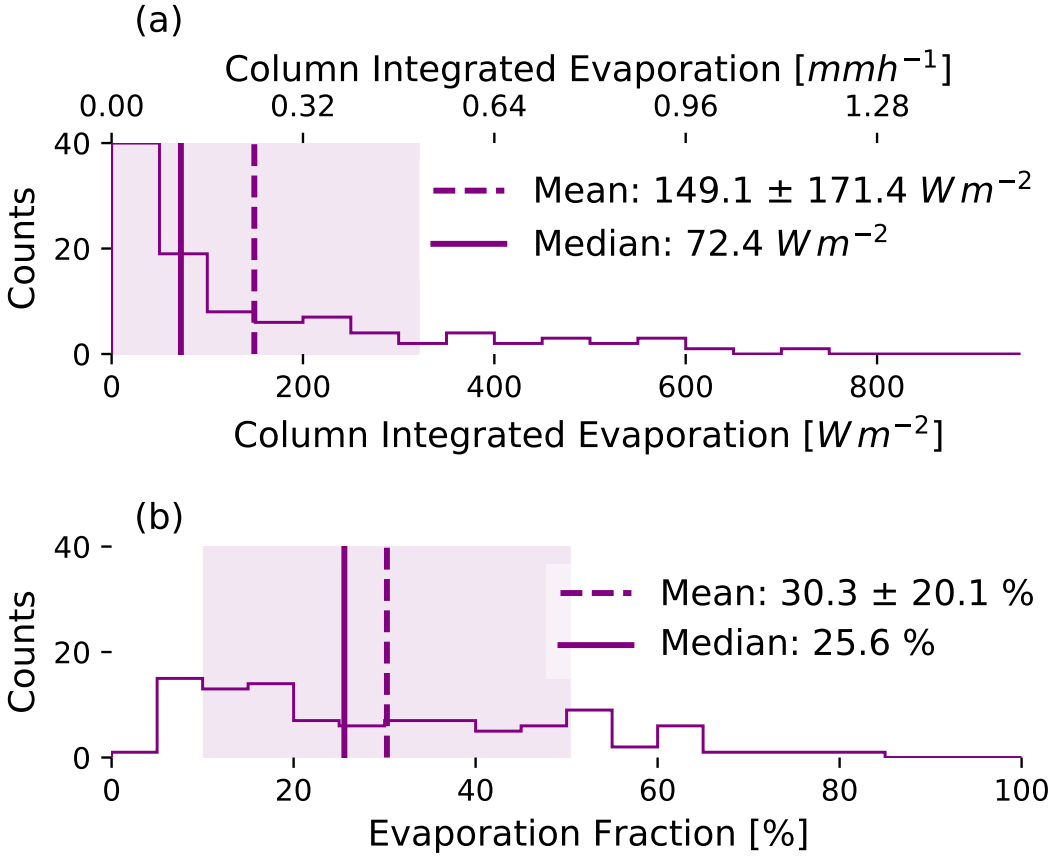

Figure 4. Histograms of (a) column integrated evaporative cooling and (b) evaporation fraction for the EvapOnly setup. Mean denoted as dashed vertical line with standard deviation as shading. Median as solid vertical line. Values are shown in the legend.

We have varying degrees of agreement with the shallow cumuli modeled by Sarkar et al. (2023). Our column integrated evaporative cooling rates are higher than, but comparable to, the results of Sarkar et al. (2023), who identified a range of $15 - 352\ \mathrm{W\ m^{-2}}$ (comparable also with various measurement campaigns they mention, around $100\ \mathrm{W\ m^{-2}}$). However, our estimated evaporation fraction is much lower than their average of 63%. Accordingly, whilst we observe bottom-heavy evaporation profiles far more frequently than top-heavy ones, Sarkar et al. (2023) reported that top-heavy profiles were more common. We discuss plausible reasons for these discrepancies in Section 3.1.

3.1 What controls the evaporation profile, rate and fraction?

In this section, we explore potential factors shaping sub-cloud rain evaporation focusing on the role of cloud-base precipitation, the cloud-base droplet size distribution and the sub-cloud layer relative humidity profile. Cloud-base precipitation is strongly

https://doi.org/10.5194/egusphere-2025-5551
Preprint. Discussion started: 5 December 2025

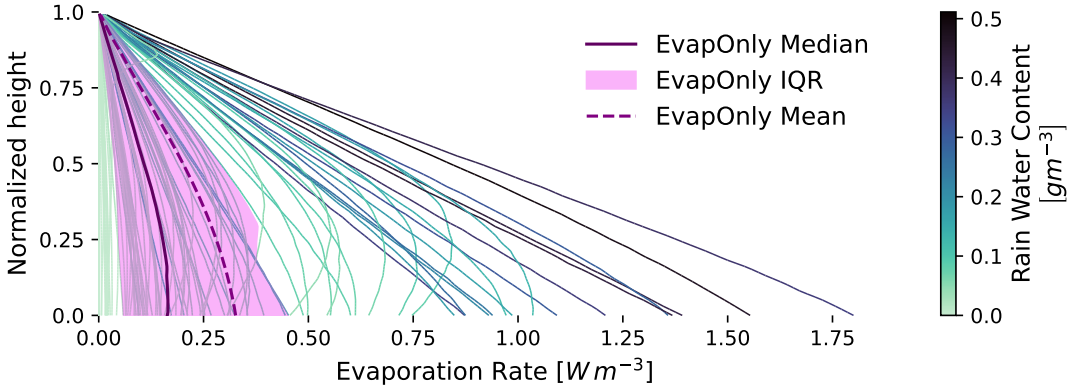

Figure 5. Profile of the evaporative cooling rate against height for each cloud in the EvapOnly setup, normalized by each cloud's cloud-base height and colored by rain water content at the corresponding normalized height (thin lines). The mean (dashed purple line), median (solid dark purple line) and IQR (purple shading) are also shown.

correlated to cloud-base RWC via the droplets' fall speed, and so the results presented here for cloud-base RWC qualitatively also hold for cloud-base precipitation. The cloud-base DSD is well characterized by its mean mass radius, $\overline{r_{\mathrm{M}}}$. Therefore, we begin by investigating how the evaporative cooling rate and the evaporation fraction of our clouds are related to the relative humidity, cloud-base RWC and $\overline{r_{\mathrm{M}}}$. We present the results for the EvapOnly, "control", setup, and examine the effect of collisions between droplets afterwards in Section 3.2.

To first order cloud-base RWC controls the amount of sub-cloud rain evaporation. Figure 5 shows that below all clouds, RWC decreases towards the surface due to evaporation. Moreover clouds with higher cloud-base RWC, i.e. higher cloud-base precipitation flux, induce more evaporation, as seen both in the vertical profiles in Figure 5 and integrated over the sub-cloud layer in Figure 6 (see also Figure 7a; correlation of $R = 0.90$ between cloud-base RWC and column integrated evaporative cooling). The higher the RWC at cloud-base, the more rain mass is available to evaporate in the sub-cloud layer. The remaining variance in evaporation can be explained by the diversity of DSDs and relative humidity profiles in our cloud sample.

The vertical gradient of evaporation is mainly ruled by the relative humidity profile, outweighing the effects of RWC decreasing towards the surface and the slight increase in $\overline{r_{\mathrm{M}}}$. Figure 8 shows a strong negative correlation of the evaporative cooling rate against relative humidity with height for nearly all clouds, with an inter-cloud mean Pearson correlation coefficient of -0.94 ± 0.13. This is in line with expectations, that lower relative humidity leads to faster evaporation rates. Whilst RWC reduces towards the surface and so could cause a concurrent reduction in the evaporation rate towards the surface, we find that their correlation is negative -0.88 ± 0.16, indicating that RWC responds to rather than controls the rate of evaporation. $\overline{r_{\mathrm{M}}}$ typically increases towards the surface as the smaller droplets evaporate completely but the correlation between the vertical profile of evaporation rate and $\overline{r_{\mathrm{M}}}$ is only slightly positive and highly variable ($\mathrm{R} = 0.15 \pm 0.77$), because relative humidity is the more dominant control on the vertical gradient of rain evaporation.

https://doi.org/10.5194/egusphere-2025-5551
Preprint. Discussion started: 5 December 2025

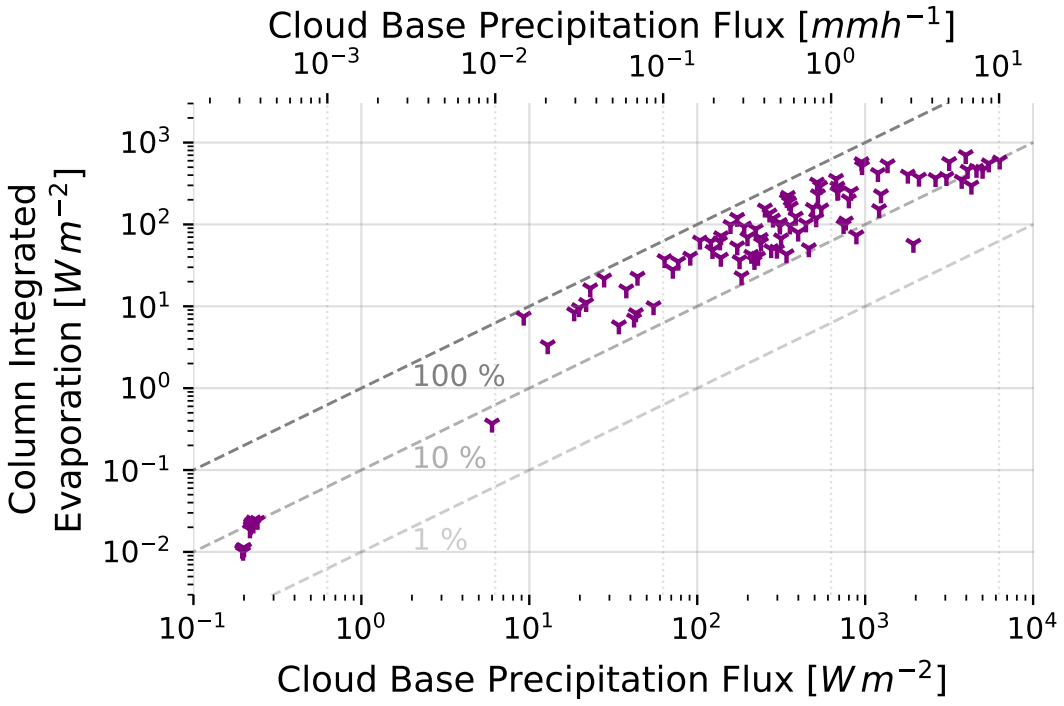

Figure 6. Column integrated evaporative cooling against cloud-base precipitation flux for the EvapOnly setup. Dashed lines indicate contours of evaporation fraction of $100, 10, 1\%$.

Whilst the vertical profile of relative humidity shapes the profile of evaporation, the relative humidity does not appear to impact the column integrated (i.e. total) evaporative cooling strongly ($\mathrm{R} = 0.01$; Figure A3i). This may be because the fitted thermodynamic profiles do not vary sufficiently enough between clouds to cause appreciable differences in the total evaporation rate. We expect that for profiles in much more diverse environments, the impact of mean relative humidity would be greater, e.g. as shown by Srivastava (1985, 1987).

The mean evaporation height, a measure of the top-/bottom-heaviness of the evaporation profile, depends most strongly on $\overline{r_{\mathrm{M}}}$ (Figure A3k). The correlation between $\overline{r_{\mathrm{M}}}$ and the mean evaporation height is negative for small $\overline{r_{\mathrm{M}}}$ because increasing $\overline{r_{\mathrm{M}}}$ in this regime reduces the number of droplets which completely evaporate higher in the column. Therefore clouds with smaller $\overline{r_{\mathrm{M}}}$, have a more curved, top-heavy evaporation profile, similar to the profiles found by Sarkar et al. (2023). Meanwhile for larger $\overline{r_{\mathrm{M}}}$, above about $750\ \mu\mathrm{m}$, the mean evaporation height shows little correlation with $\overline{r_{\mathrm{M}}}$ since so few droplets completely evaporate. We also find very little impact of the cloud-base height on the evaporation fraction and column integrated evaporation (Figure A3e,j,o).

https://doi.org/10.5194/egusphere-2025-5551
Preprint. Discussion started: 5 December 2025

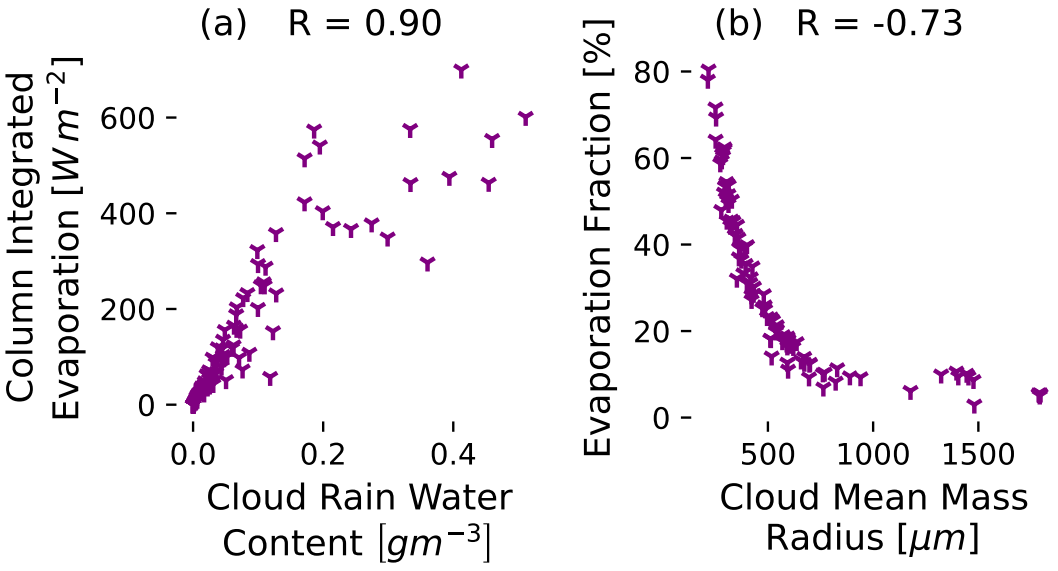

Figure 7. The leading controls on sub-cloud layer evaporation for our sample of clouds, and their Pearson correlation coefficients. Each marker indicates an individual cloud. (a) Column integrated evaporative cooling is predominately controlled by the cloud-base RWC; (b) Evaporation fraction is predominately controlled by the cloud-base DSD, well-captured by the cloud-base mean mass radius, $\overline{r_{\mathrm{M}}}$. (Additional correlations are also shown in Figure A3.)

The evaporation fraction is fundamentally ruled by raindrop size distribution at cloud-base. Higher $\overline{r_{\mathrm{M}}}$ implies larger droplets in the cloud-base DSD, which evaporate less efficiently and thus lower the evaporation fraction. Thus, for the same RWC, a cloud with smaller $\overline{r_{\mathrm{M}}}$ will have a higher evaporation fraction. Figure 7b shows this relation of the evaporation fraction to $\overline{r_{\mathrm{M}}}$, albeit the Pearson correlation coefficient underestimates the non-linear relation of the two variables ($R = -0.73$). Figure 9 shows the same relation as well as an analytical single-droplet, mean-field approximation for the evaporation fraction. This approximation predicts that the evaporation fraction of a single droplet falling through a rainshaft with mean relative humidity and temperature scales with its radius as $r^{-7/4}$ (Appendix A). The approximation is well in line with the results of our SDM for most clouds with $\overline{r_{\mathrm{M}}}$ between $150 - 1000$ µm. The exceptions are clouds with broad DSDs, which, as expected, cannot be approximated well by a single radius and whose shape changes significantly with height. The spread amongst clouds with similar $\overline{r_{\mathrm{M}}}$ but which still comply with the approximation can be explained by their slightly different relative humidity profiles and DSD widths. Since these differences are very small, the mean mass radius $\overline{r_{\mathrm{M}}}$ of a DSD can be used to estimate the evaporation fraction well.

Figure 9 also shows that accounting for the ventilation effect (the increase in evaporation rate due to droplet motion; Pruppacher and Klett (2010); Bayley et al. (2025b)) is crucial for modeling evaporation. Ventilation increases the evaporation rate of large raindrops significantly — roughly by a factor 9 for radii of 1 mm, and so omitting ventilation strongly reduces evaporation for all the clouds, with the strongest reduction for clouds with high $\overline{r_{\mathrm{M}}}$. The size dependence of the evaporation fraction

https://doi.org/10.5194/egusphere-2025-5551
Preprint. Discussion started: 5 December 2025

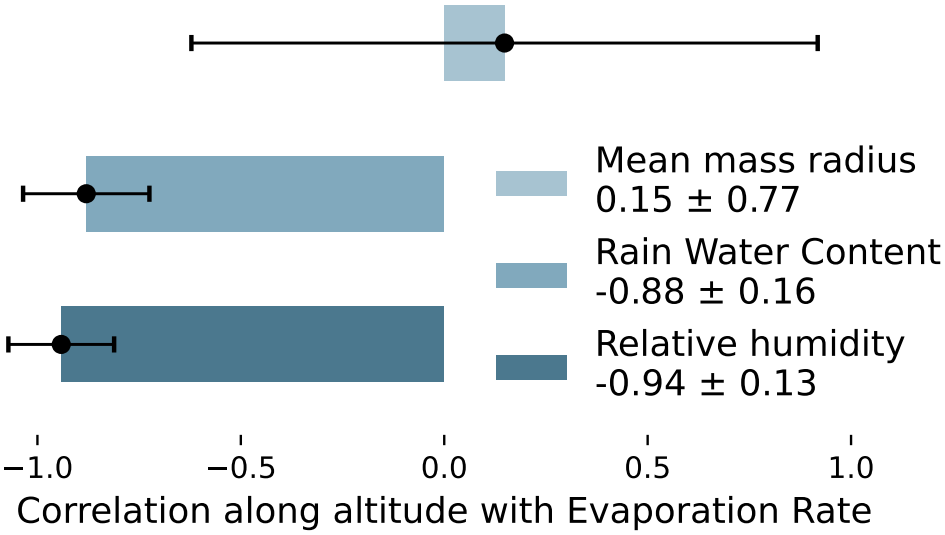

Figure 8. Histogram shows the intercloud mean Pearson correlation coefficients along altitude between evaporation rate and relative humidity (dark blue), RWC (blue) and $\overline{r_{\mathrm{M}}}$ (light blue) based on all simulated clouds for the EvapOnly setup. Respective inter-cloud mean and standard deviation of Pearson correlation coefficients shown in the legend.

is proportional to the ventilation coefficient f_v (Appendix A). As such, setting $f_v = 1$ changes the evaporation fraction to scale with $r^{-5/2}$ instead of $r^{-7/4}$. Neglecting the ventilation effect, as is often done in microphysics models, therefore has serious implications for sub-cloud energetics and the formation of simulated cold pools.

The lower evaporation fraction, higher column integrated evaporative cooling, and more bottom-heavy vertical profiles that we have found compared to Sarkar et al. (2023), are likely explained by our observations being downstream of theirs. Further downstream in the trades rain tends to be more abundant and stronger, resulting in measurements with higher RWC and larger $\overline{r_{\mathrm{M}}}$. Sarkar et al. (2023) prescribed cloud-base DSDs with a $\overline{r_{\mathrm{M}}}$ as low as $0.1\ \mathrm{mm}$, whilst $\overline{r_{\mathrm{M}}}$ of our distributions lies between $0.2 - 2\ \mathrm{mm}$. Therefore, we expect our simulations to show lower evaporation fractions and more bottom-heavy evaporation. In addition, the higher RWC of our clouds leads to higher column integrated evaporative cooling. These differences highlight the major significance of cloud DSDs and their approximations for estimating evaporation rates in the sub-cloud layer of shallow-clouds.

3.2 Effect of Collisions Between Droplets

Collisions between raindrops induce systematic but only minor differences in rain evaporation for the clouds studied here. Figure 10 shows the relative differences of the evaporation rate profiles between the setups accounting for collisions and the EvapOnly

https://doi.org/10.5194/egusphere-2025-5551
Preprint. Discussion started: 5 December 2025

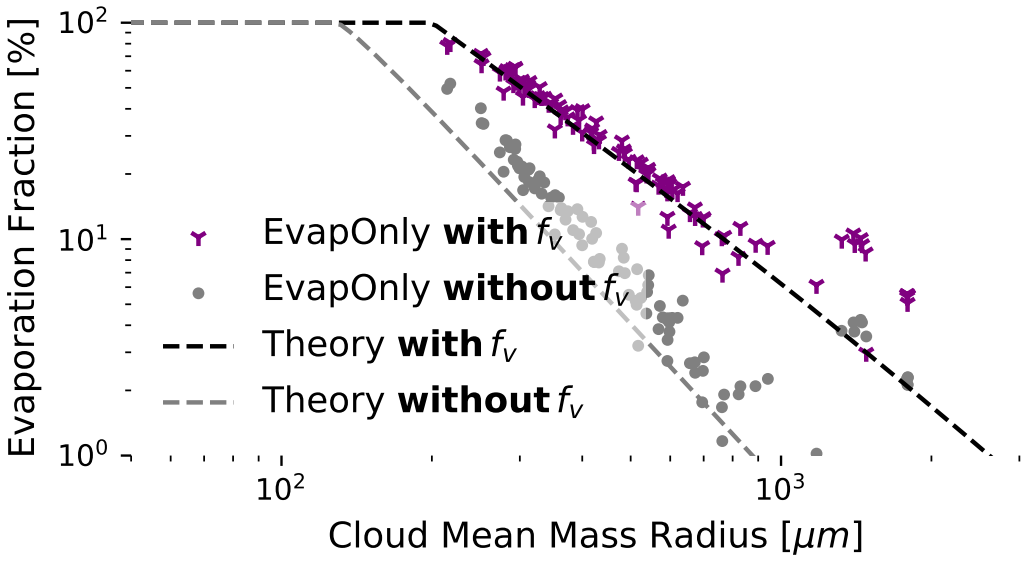

Figure 9. Evaporation fraction against cloud-base $\overline{r_{\mathrm{M}}}$ for all clouds in the EvapOnly setup (purple tri-blade markers). The Dashed black line shows the single-droplet analytical approximation for Köhler theory accounting for ventilation effects. The gray dots and gray dashed line show the same simulations and theory but neglecting the ventilation effect.

setup. The percentile shading also indicates a modest spread across the clouds simulated, which increases towards the surface because the differences induced at higher altitudes are propagated downwards and thus accumulate through the rainshaft.

Including collision-coalescence (EvapCoal) decreases the mean and median by up to 5% near the surface compared to the evaporation/condensation-only setup (Figure 10a). However, including breakup and rebound as well as coalescence in the EvapCoalBuRe-few setup, opposes the coalescence effect and leads to a mean profile similar to the EvapOnly setup (Figure 10b). If anything, the slight negative skew of the change in evaporation profiles compared to EvapOnly shows the combined effect of breakup, rebound and coalescence is more likely to increase evaporation for a population of clouds, however, for individual clouds it is not clear-cut whether the combined effect leads to more or less evaporation. It depends on the DSD, because the DSD controls the probability with which these three outcomes occur. Collisional breakup is more likely in broader distributions with larger $\overline{r_{\mathrm{M}}}$, and this favors the increase of evaporation for these clouds because it creates more, and smaller droplets. Vice versa for narrower DSDs with smaller $\overline{r_{\mathrm{M}}}$ whereby collision-coalescence is favoured which produces larger droplets that evaporate less efficiently.

Except for in cases of extreme breakup, the variability among our sample of shallow cumuli exceeds the impact of collisions on evaporation. The mean and standard deviation of the evaporation fraction and column integrated evaporative cooling are nearly identical for EvapCoal and EvapCoalBuRe-few setups, compared to EvapOnly values of $30 \pm 20\%$ and $150 \pm 170\ \mathrm{W\ m^{-2}}$

https://doi.org/10.5194/egusphere-2025-5551
Preprint. Discussion started: 5 December 2025

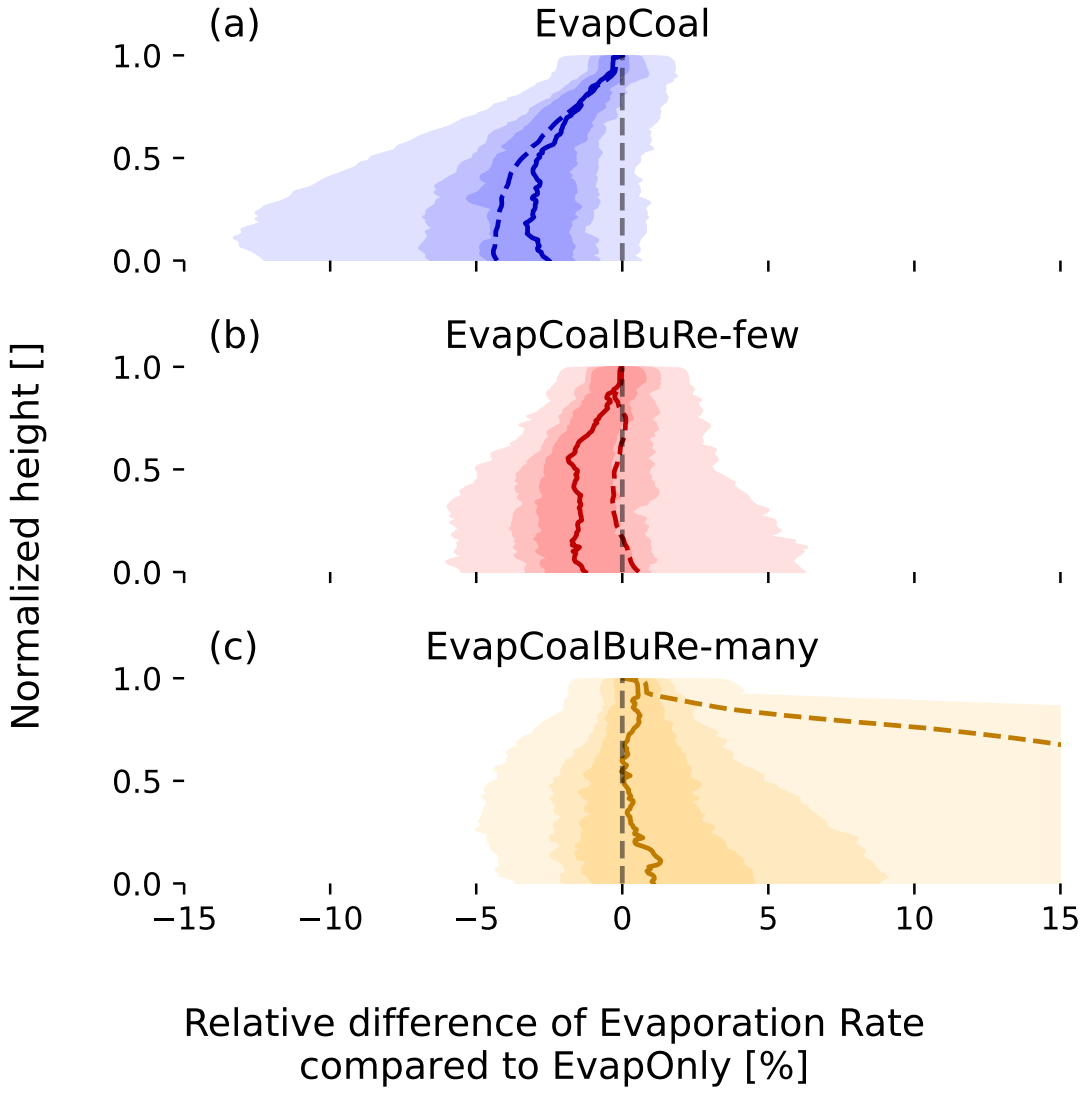

Figure 10. Relative difference of evaporation profiles of (a) EvapCoal, (b) EvapCoalBuRe-few, (c) EvapCoalBuRe-many, compared to EvapOnly setup. Inter-cloud mean as dashed line. Inter-cloud median as solid line. Percentile range as shadings from dark to light are $33-66\%$, $25-75\%$ and $10-90\%$.

respectively (Figure A1a). The values for the EvapCoalBuRe-many setup, at 220 ± 360 W m^{-2} and $32 \pm 18\%$, are higher, because a few clouds undergo very extreme breakup in the sub-cloud layer which enhances evaporation there (Figure A1a).

The lower tail of the distribution of vertical evaporation rates does not change when more fragments are produced during breakup (EvapCoalBuRe-many compared to EvapCoalBuRe-few), but the upper tail increases substantially (Figure 10c). The upper tail contains the few clouds for which breakup occurs frequently and here we see increases the mean evaporation rate in the

https://doi.org/10.5194/egusphere-2025-5551
Preprint. Discussion started: 5 December 2025

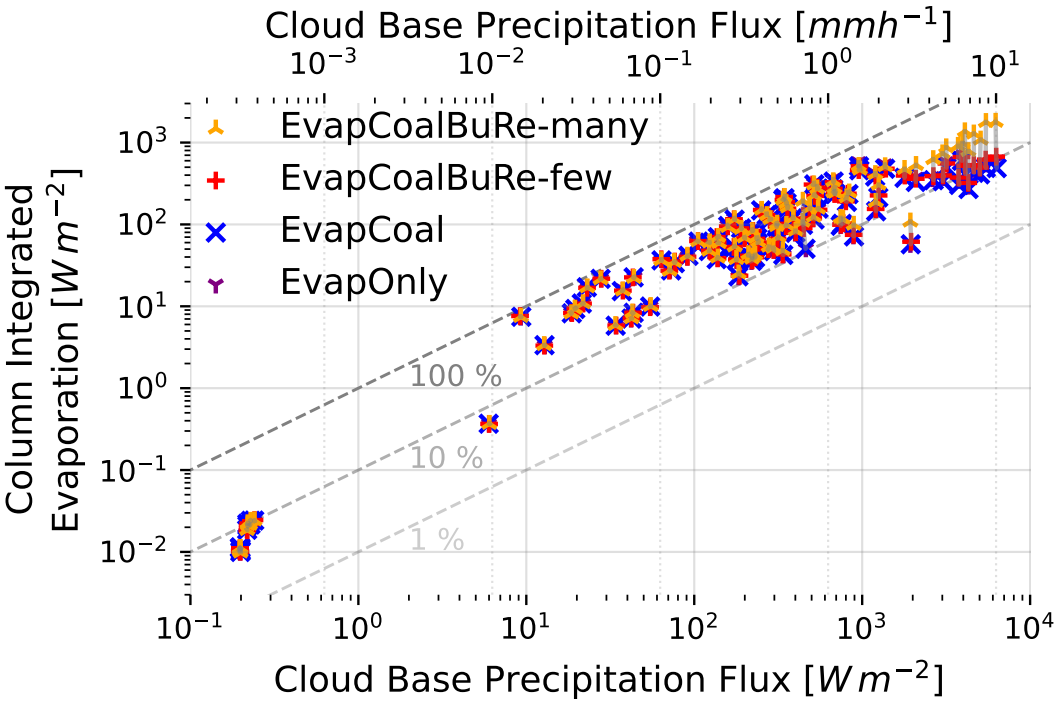

Figure 11. As Figure 6 but showing results for all microphysical setups with markers and colors as indicated in the legend. Dashed lines indicate contours of evaporation fraction of $100, 10, 1\%$. The four setups for an individual cloud are connected by a thin grey line.

sub-cloud layer by 70% relative to the evaporation/condensation-only setup. Since EvapCoalBuRe-many drastically increases the number of fragments, to the extreme, these results can be considered an upper bound to the effect of breakup on evaporation rates beneath shallow cumuli in a more realistic setting.

Larger cloud-base precipitation fluxes lead to larger differences between the setups which account for collisions and the setup which only accounts for evaporation/condensation, differences both in evaporation fraction and column integrated evaporative cooling. In general, clouds with cloud-base precipitation above $2000\ \mathrm{W\ m^{-2}}$, roughly corresponding to $3\ \mathrm{mm\ h^{-1}}$ and $1\ \mathrm{g\ m^{-3}}$ RWC, are more affected by collisions both in their column integrated evaporative cooling and in their evaporation fraction (Figure 11, also Figure A2a, c), especially in cases of extreme breakup. These results suggest that, although droplet collisions negligibly impact evaporation beneath the shallow trade-wind cumuli we have simulated, it's role becomes increasingly important as clouds deepen and their DSDs widen. We thus expect droplet collisions to play a greater role in controlling evaporation rates for more heavily precipitating clouds.

https://doi.org/10.5194/egusphere-2025-5551
Preprint. Discussion started: 5 December 2025

4 Summary and Outlook

4.1 Summary

Bridging the gap between field data and modeling, we use a superdroplet model (SDM) for cloud microphysics in conjunction with observations from the EUREC^{4}A field campaign to estimate the strength of, and controls on, evaporation in the sub-cloud layer of precipitating trade-wind shallow cumuli. We identified 102 distinct clouds from the observations, with cloud-base DSDs from in-situ measurements and thermodynamic profiles from dropsonde measurements and used them to setup a steady-state 1-D rainshaft model so that we could analyse the evaporative cooling and evaporation fraction in the sub-cloud layer, in a way that is more directly comparable to observations than idealized studies. By using SDM, we represent all droplets without the need for arbitrary condensate categorization or any assumption on the droplet size distribution in the sub-cloud layer. Furthermore, we have a clear link between our model and the fundamental theories of cloud microphysics, meaning we can apply Köhler theory for condensation/evaporation explicitly, without being confounded by numerical diffusion, and we can test the impact of collision coalescence, rebound and breakup on rain evaporation for the first time.

Simulating only evaporation/condensation and droplet motion we estimate the column integrated evaporative cooling for our sample of clouds ranges from $0 - 800\ \mathrm{W\ m^{-2}}$, with a mean of $150 \pm 170\ \mathrm{W\ m^{-2}}$ and a median of $72\ \mathrm{W\ m^{-2}}$. Evaporated fraction ranges from $0 - 80\%$ and is less skewed, with a mean of $30 \pm 20\%$ and a median of 25.6%. These values are in the same range as those of (Sarkar et al., 2023, 2025), who also estimated rain evaporation from precipitating shallow-clouds, but with a bin microphysics scheme based on observations from another aircraft of the EUREC^{4}A/ATOMIC campaign.

Based on our cloud sample we identified three key controls on rain evaporation in the sub-cloud layer. Cloud-base rain water content (RWC) rules the column integrated evaporative cooling and explains most of the variance across our sample ($R = 0.90$), in agreement with Sarkar et al. (2023) and Sarkar et al. (2025). Relative humidity determines the overall gradient of the evaporation profiles with a mean correlation along altitude of $R = -0.94 \pm 0.13$. Our results show more bottom-heavy evaporation than Sarkar et al. (2023), which can be explained by our DSDs having larger mean mass radii, $\overline{r_\mathrm{M}}$. The role of $\overline{r_\mathrm{M}}$ in shaping the top-/bottom-heaviness of the profiles also aligns with our finding that $\overline{r_\mathrm{M}}$ is the key control on the evaporation fraction — as expected because larger droplets evaporate less efficiently. For narrow DSDs we can also match our evaporation fraction with a single-droplet mean-field approximation that has an analytical form.

For the first time, the effect of droplet collisions: coalescence, breakup, and rebound, on sub-cloud rain evaporation could be estimated. By using SDM we run all 102 cloud simulations under four different microphysical scenarios: excluding collisions (EvapOnly), including additionally collision-coalescence (EvapCoal), and further including rebound and breakup with either very few, or very many fragments produced in the event of breakup (EvapCoalBuRe-few and EvapCoalBuRe-many respectively). Including collisions in any scenario played a negligible role in our precipitating shallow-clouds sample, meaning that under light rain conditions, simplified microphysics which only considers condensation/evaporation is justified, as long as it accounts for ventilation effects. Nevertheless, we cannot rule out the importance of droplet collisions for more heavily precipitating clouds that have more than $2000\ \mathrm{W\ m^{-2}}$ cloud-base precipitation, roughly corresponding to $3\ \mathrm{mm\ h^{-1}}$ and $1\ \mathrm{g m^{-3}}$ RWC. For these clouds, the reduction in evaporation may easily exceed 10% if coalescence is included. Including breakup and rebound addi-

https://doi.org/10.5194/egusphere-2025-5551
Preprint. Discussion started: 5 December 2025

tionally reduces the impact of coalescence, and may even enhance rain evaporation, depending on the details of collisional breakup.

4.2 Outlook

Our results point to the importance of the DSD on evaporation beneath shallow-clouds. Clouds with similar cloud-base precipitation can produce different evaporation profiles solely due to differences in the shape of the DSD. The most likely reason for our lower evaporation fraction, higher column integrated evaporative cooling, and more bottom-heavy vertical profiles which we observe compared to Sarkar et al. (2023) is the higher RWC and larger $\overline{r_M}$ of our cloud-base distributions. This points to the importance of accurately representing DSDs and their evolution, which requires not just a highly resolved microphysics scheme (SDMs, bin schemes, or many-moment bulk schemes), but also accurate observations and a suitable fit to model them. In the future, assuming the functional form of the DSD we use in models should also be avoided, since how they distort the observed DSD likely distorts the evaporation that is modeled too (Igel and Van Den Heever, 2017a, b).

It is encouraging that collisions play only a minor role in controlling evaporation for our cloud sample, but it is still unclear how heavily precipitating cases are affected. Since microphysics schemes tend to agree on the evolution of the DSD in the absence of collisions (Hill et al., 2023), it should be possible to achieve a broad consensus for evaporation rates beneath shallow-clouds, even including cruder models, as we show with our single-droplet analytical approximation (accounting for ventilation effects). What remains to be seen is whether this is true for a wider set of environmental and microphysical conditions than our sample allowed, especially more heavily precipitating cases. For this we require more long-term observations, which sample a more variable cloud population. We also require a clearer understanding of how to model droplet breakup because the uncertainties in the fragment size distribution prevent us from tightly constraining breakup's effect on rain evaporation. For heavier precipitation than we have sampled, models may have to account not only for the feedback of microphysics onto the relative humidity profile, which could amplify the role of collisions on evaporation rates, but also the impact of evaporation on turbulent mixing and buoyancy; both of which a non-steady-state rainshaft could capture.

Whilst we only studied precipitating trade-wind shallow cumuli observed during EUREC^{4}A, our model is ready to be applied to any analogous observational datasets. This opens the door to its use on long-term measurements and to comparison with radar-based retrievals of rain evaporation (Tridon et al., 2017). A larger record of rain evaporation, which involves more clouds also under different environmental conditions, is needed to confirm that differences in our cloud samples cause the differences between our results and those of Sarkar et al. (2023). Such a record could also be used to extend our analysis to different cloud regimes. Measurements from the Barbados Cloud Observatory (Stevens et al., 2016) are well-suited to this task, as they span the range of shallow and deep convection typical of the dry and wet seasons in the tropics. Understanding and accurately modeling rain evaporation is crucial for predicting cold pool formation and cloud cover in the trades; our study provides new constraints on this process and in conjunction with further observations can improve how models represent shallow convection and its feedbacks in the climate system.

https://doi.org/10.5194/egusphere-2025-5551
Preprint. Discussion started: 5 December 2025

Code availability. CLEO is published on it's GitHub page: https://github.com/yoctoyotta1024/CLEO, alongside it's documentation: https://yoctoyotta1024.github.io/CLEO. Version v0.39.7 is used in this study and was described and tested in Bayley et al. (2025b).

Code and data availability. The code to preprocess the observational data and to perform the fitting is published on the GitHub page: https://github.com/nilsnevertree/sdm-eurec4a. This repository also includes code to post-process the output data of the CLEO simulations and to produce the figures we use here. Post-processed simulation data can be provided upon reasonable request to the authors.

Appendix A: Single-Droplet Mean-Field Approximation of Evaporation fraction

We consider an evaporating droplet of initial radius r_0 and mass m_0 falling in sub-saturated air ($q_v < q_{v,\mathrm{sat}}$) from an initial height H. In classical evaporation theory (Langmuir., 1918; Pruppacher and Klett, 2010), the radius r of the droplet evolves as

$$\frac{\mathrm{d}r^2}{\mathrm{d}t} = -2D_* f_v \frac{\rho}{\rho_w}(q_{v,\mathrm{sat}} - q_v), \tag{A1}$$

with

$$D_* = D_v \Bigg/ \left[1 + \frac{\ell_v D_v \rho_{v,\mathrm{sat}}}{k_a T}\left(\frac{\ell_v}{R_v T} - 1\right)\right]. \tag{A2}$$

D_v is the molecular diffusivity of water vapor in air, ℓ_v the enthalpy of vaporization, k_a the thermal conductivity of air, f_v the ventilation coefficient, and R_v the gas constant for water vapor. We neglect curvature and solute effects, which are negligible above $\sim 10\ \mu\mathrm{m}$. D_* is an effective diffusion coefficient that takes into account the thermal effects of evaporation (Pruppacher and Klett, 2010).

We assume in this section that the droplet moves at its terminal velocity $U(r)$ at all times, which is reasonable on time scales longer than a few milliseconds. Numerical integration of the full equations of motion for a single droplet (not shown here) shows that the droplets are always within 0.01% of their terminal velocities, except near the very end of their trajectories if they evaporate completely. The height of the droplet can then be expressed as $\mathrm{d}z = -U(r)\mathrm{d}t$, so that equation (A1) becomes

$$\frac{\mathrm{d}r^2}{\mathrm{d}z} = 2\frac{D_* f_v(r)}{U(r)}\frac{\rho}{\rho_w}(q_{v,\mathrm{sat}} - q_v). \tag{A3}$$

We assume the vertical profiles of T and q_v to be uniform. Between cloud-base height H and the ground where $r(z=0) = r_f$, equation (A3) then transforms into

$$\int_{r_0}^{r_f} \frac{U(r)}{f_v(r)} r\mathrm{d}r = -D_* H \frac{\rho}{\rho_w}(q_{v,\mathrm{sat}} - q_v) \tag{A4}$$

Exact closed-form solutions are difficult to find as they are set by the functional dependence of U and f_v with r. We can find an approximation in the low evaporation limit where $\xi \ll 1$ and the integral simplifies at first order, since U/f_v varies weakly:

$$\int_{r_0}^{r_f} \frac{U(r)}{f_v(r)} r\mathrm{d}r \simeq \frac{U(r_0)}{f_v(r_0)} r_0 (r_f - r_0) \tag{A5}$$

https://doi.org/10.5194/egusphere-2025-5551
Preprint. Discussion started: 5 December 2025

so that

$$r_0 - r_f = \Delta r = D_* H \frac{f_v(r_0)}{U(r_0) r_0} \frac{\rho}{\rho_w} (q_{v,\mathrm{sat}} - q_v). \tag{A6}$$

The evaporation fraction ξ reads

$$\xi = \frac{m_0 - m_f}{m_0} = \frac{r_0^3 - r_f^3}{r_0^3} = 1 - \left(1 - \frac{\Delta r}{r_0}\right)^3, \tag{A7}$$

which approximates, in the limit of $\Delta r \ll r_0$, to

$$\xi \simeq 3\frac{\Delta r}{r_0} \simeq 3 D_* H \frac{f_v(r_0)}{U(r_0) r_0^2} \frac{\rho}{\rho_w} (q_{v,\mathrm{sat}} - q_v). \tag{A8}$$

The dependence of the evaporation fraction with size is thus set by the size dependence of the ventilation coefficient and the terminal velocity. The terminal velocity can be reasonably approximated to be $U(r) = b\sqrt{r}$ between $500\ \mu\mathrm{m}$ and $2\ \mathrm{mm}$. In the case of no ventilation effect ($f_v = 1$), this sets a power law dependence $\xi \propto r_0^{-5/2}$ in this limit. The ventilation coefficient varies as $f_v \propto N_{\mathrm{Re}}^{1/2}$ with $N_{\mathrm{Re}} \propto U(r_0) r_0$ the Reynolds number of the droplet (Pruppacher and Klett, 2010). This gives $\xi \propto r_0^{-7/4}$ when ventilation is taken into account.

https://doi.org/10.5194/egusphere-2025-5551
Preprint. Discussion started: 5 December 2025

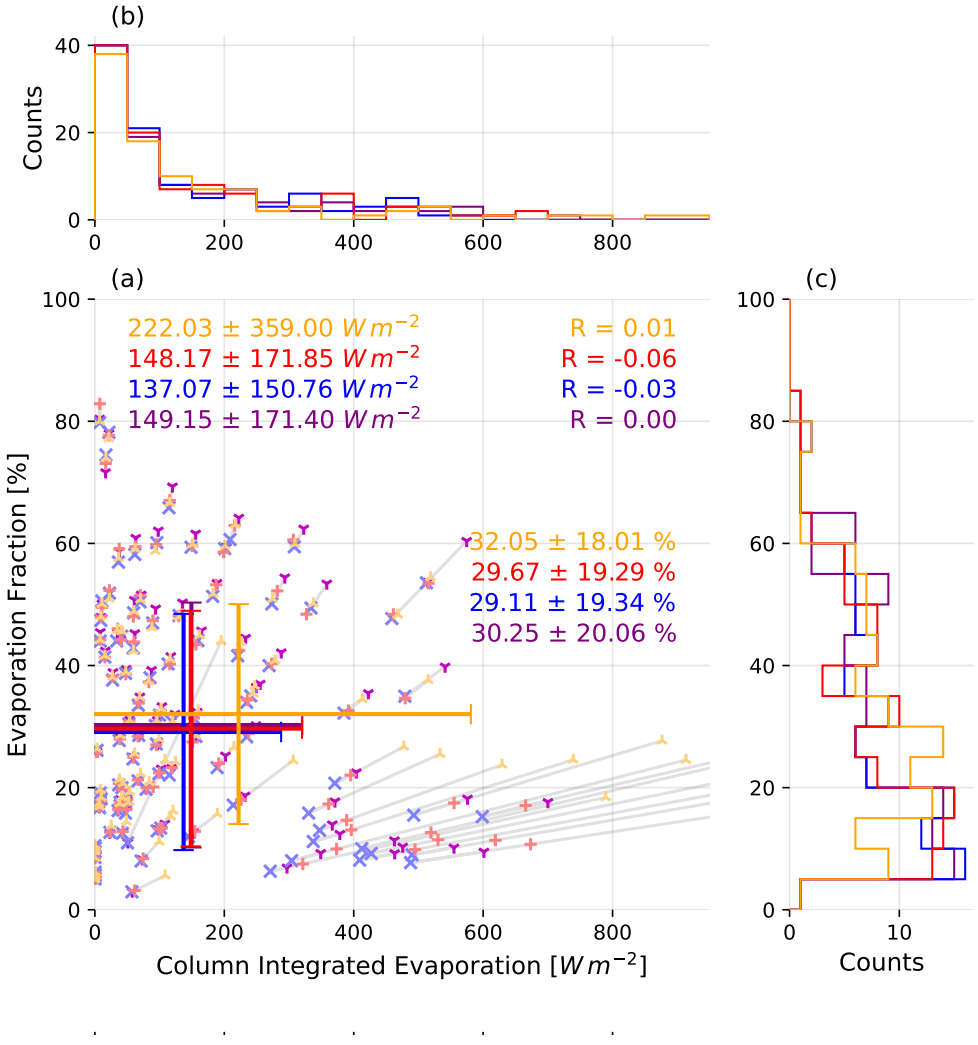

Figure A1. (a) Evaporation fraction against column integrated evaporative cooling for individual clouds and all microphysics setups. Colors and markers as in Figure 11 (EvapOnly in purple, EvapCoal in blue, EvapCoalBuRe-few in red and EvapCoalBuRe-many in orange). Simulations for the same cloud are connected by thin grey lines. Big error bars denote inter-cloud mean and standard deviation, both values denoted at top left and bottom right (Top to bottom: EvapCoalBuRe-many, EvapCoalBuRe-few, EvapCoal and EvapOnly). (b) Histogram of evaporation fraction for all microphysics setups. (c) Histogram of column integrated evaporative cooling for all microphysic setups.

https://doi.org/10.5194/egusphere-2025-5551
Preprint. Discussion started: 5 December 2025

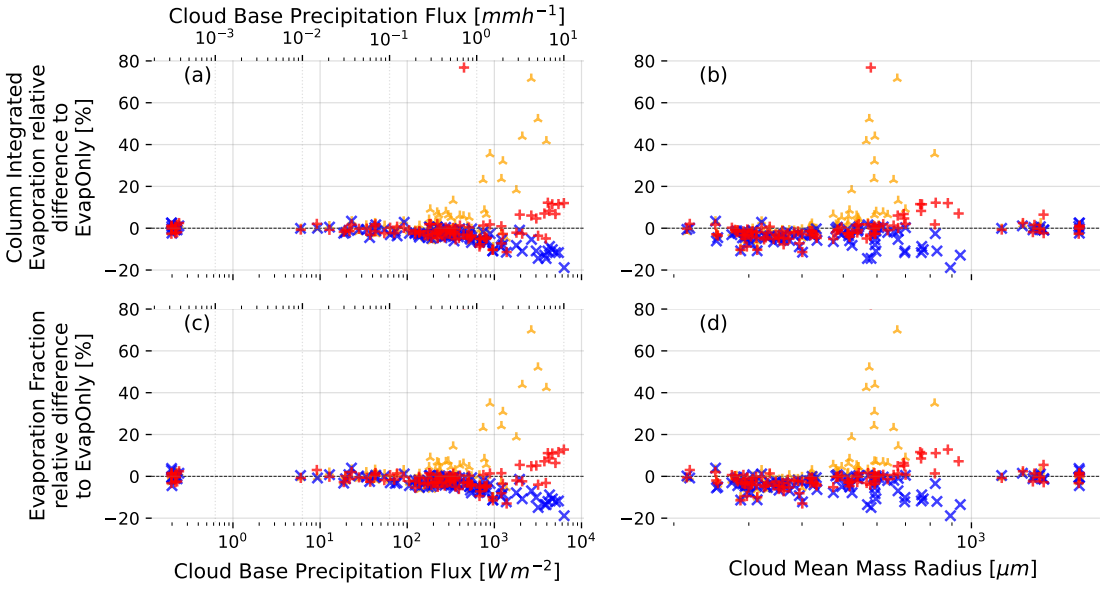

Figure A2. Relative differences between EvapCoal and EvapCoalBuRe-few against EvapOnly of column integrated evaporative cooling (a,b) and evaporation fraction (c,d) compared to cloud-base precipitation flux (a,c) and cloud mean mass radius (b,d).

https://doi.org/10.5194/egusphere-2025-5551
Preprint. Discussion started: 5 December 2025

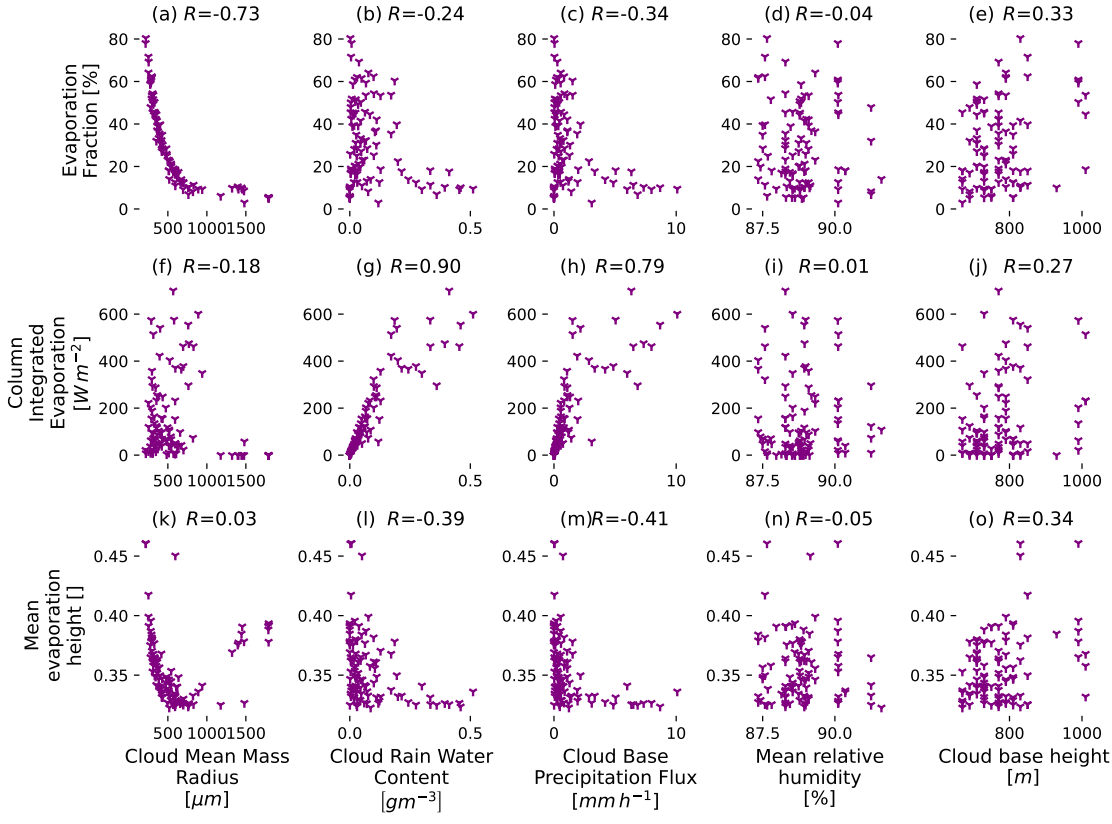

Figure A3. Scatter of (a-e) evaporation fraction, (f-j) column integrated evaporative cooling and (k-o) mean evaporation height against various cloud and environmental variables.

https://doi.org/10.5194/egusphere-2025-5551
Preprint. Discussion started: 5 December 2025

Author contributions. NN fitted the observational data, ran the model, and processed the output. CJAB was the main developer of CLEO for the project; she constructed the model setups and worked collaboratively with NN to interpret the results, and to write and edit the manuscript. RV and CJAB conceptualized the project, and RV oversaw the project's development and had many discussions with CJAB and NN to discuss the observations, the results, and the manuscript. FP contributed the single-droplet analytical approximation to the results. AKN and MP provided scientific support, interpretation of results and feedback on the manuscript.

Competing interests. CJAB declares that none of the authors have any competing interests.

Acknowledgements. Many thanks to the members of the rain evaporation club for our productive discussions. Thanks also to Shin-ichiro Shima (University of Hyogo, Japan) for his advice on the model setup and constructive feedback on the initial version of the manuscript. C. J.A. Bayley further expresses their appreciation for the work of the developers of the free and open-source software which underlies CLEO, especially from the developers of Git, GitHub, Python, the C++ standard libraries, and, above all, Kokkos.

R. Vogel acknowledges support from an ERC starting grant (ROTOR, grant no. 101116282). N. Niebaum, F. Poydenot and R. Vogel have further received funding from the Deutsche Forschungsgemeinschaft (DFG, German Research Foundation) under Germany's Excellence Strategy - EXC 2037 "Climate, Climatic Change, and Society" (project number 390683824)

A. K. Naumann has received funding which supported this work from the Deutsche Forschungsgemeinschaft (DFG, German Research Foundation) under Germany's Excellence Strategy - EXC 2037 "Climate, Climatic Change, and Society" (project number 390683824)

We thank the Deutsche Klimarechenzentrum (DKRZ) and the Gesellschaft für wissenschaftliche Datenverarbetitung mbH Göttingen (GWDG) for the use of their computer facilities and software to conduct our work.

https://doi.org/10.5194/egusphere-2025-5551
Preprint. Discussion started: 5 December 2025

References

Acquistapace, C., Coulter, R., Crewell, S., Garcia-Benadi, A., Gierens, R., Labbri, G., Myagkov, A., Risse, N., and Schween, J. H.: EUREC^{4}A's *Maria S. Merian* ship-based cloud and micro rain radar observations of clouds and precipitation, Earth System Science Data, 14, 33–55, https://doi.org/10.5194/essd-14-33-2022, publisher: Copernicus GmbH, 2022.

Alinaghi, P., Siebesma, P., Jansson, F., Janssens, M., and Glassmeier, F.: External Drivers and Mesoscale Self-Organization of Shallow Cold Pools in the Trade-Wind Regime, Journal of Advances in Modeling Earth Systems, 17, e2024MS004 540, https://doi.org/10.1029/2024MS004540, 2025.

(AMS), A. M. S.: raindrop - Glossary of Meteorology, https://glossary.ametsoc.org/wiki/Raindrop, 2025.

Andrejczuk, M., Grabowski, W. W., Reisner, J., and Gadian, A.: Cloud-aerosol interactions for boundary layer stratocumulus in the Lagrangian Cloud Model, Journal of Geophysical Research: Atmospheres, 115, https://doi.org/10.1029/2010JD014248, _eprint: https://onlinelibrary.wiley.com/doi/pdf/10.1029/2010JD014248, 2010.

Arabas, S., Jaruga, A., Pawlowska, H., and Grabowski, W. W.: libcloudph++ 1.0: a single-moment bulk, double-moment bulk, and particle-based warm-rain microphysics library in C++, Geoscientific Model Development, 8, 1677–1707, https://doi.org/10.5194/gmd-8-1677-2015, 2015.

Bartman, P., Bulenok, O., Górski, K., Jaruga, A., Łazarski, G., Olesik, M. A., Piasecki, B., Singer, C. E., Talar, A., and Arabas, S.: PySDM v1: particle-based cloud modeling package forwarm-rain microphysics and aqueous chemistry, Journal of Open Source Software, 7, 3219, https://doi.org/10.21105/joss.03219, 2022.

Bayley, C. J. A.: yoctoyotta1024/CLEO, https://github.com/yoctoyotta1024/CLEO, 2025.

Bayley, C. J. A., Kölling, T., Naumann, A. K., Vogel, R., and Stevens, B.: CLEO: The Fundamental Design for High Computational Performance of a New Superdroplet Model, https://doi.org/10.5194/egusphere-2025-4398, 2025a.

Bayley, C. J. A., Naumann, A. K., Poydenot, F., Vogel, R., Stevens, B., and Shima, S.-I.: CLEO: The Numerical Methods of a New Superdroplet Model including a Droplet Breakup Algorithm, https://doi.org/10.5194/egusphere-2025-4399, 2025b.

Bony, S., Stevens, B., Ament, F., Bigorre, S., Chazette, P., Crewell, S., Delanoë, J., Emanuel, K., Farrell, D., Flamant, C., Gross, S., Hirsch, L., Karstensen, J., Mayer, B., Nuijens, L., Ruppert, J. H., Sandu, I., Siebesma, P., Speich, S., Szczap, F., Totems, J., Vogel, R., Wendisch, M., and Wirth, M.: EUREC4A: A Field Campaign to Elucidate the Couplings Between Clouds, Convection and Circulation, in: Shallow Clouds, Water Vapor, Circulation, and Climate Sensitivity, edited by Pincus, R., Winker, D., Bony, S., and Stevens, B., Space Sciences Series of ISSI, pp. 357–396, Springer International Publishing, ISBN 978-3-319-77272-8, https://doi.org/10.1007/978-3-319-77273-8_16, 2018.

Bony, S., Lothon, M., Delanoë, J., Coutris, P., Etienne, J.-C., Aemisegger, F., Albright, A. L., André, T., Bellec, H., Baron, A., Bourdinot, J.-F., Brilouet, P.-E., Bourdon, A., Canonici, J.-C., Caudoux, C., Chazette, P., Cluzeau, M., Cornet, C., Desbios, J.-P., Duchanoy, D., Flamant, C., Fildier, B., Gourbeyre, C., Guiraud, L., Jiang, T., Lainard, C., Le Gac, C., Lendroit, C., Lernould, J., Perrin, T., Pouvesle, F., Richard, P., Rochetin, N., Salaün, K., Schwarzenboeck, A., Seurat, G., Stevens, B., Totems, J., Touzé-Peiffer, L., Vergez, G., Vial, J., Villiger, L., and Vogel, R.: EUREC^{4}A observations from the SAFIRE ATR42 aircraft, Earth System Science Data, 14, 2021–2064, https://doi.org/10.5194/essd-14-2021-2022, publisher: Copernicus GmbH, 2022.

Brdar, S. and Seifert, A.: McSnow: A Monte-Carlo Particle Model for Riming and Aggregation of Ice Particles in a Multidimensional Microphysical Phase Space, Journal of Advances in Modeling Earth Systems, 10, 187–206, https://doi.org/10.1002/2017MS001167, 2018.

Coutris, P.: SAFIRE ATR42: PMA/Cloud composite dataset, https://doi.org/10.25326/237, 2021.

George, G.: JOANNE-Dataset: Joint dropsonde Observations of the Atmosphere in tropical North atlaNtic meso-scale Environments (v2.0.0), https://doi.org/10.25326/246, 2021.

https://doi.org/10.5194/egusphere-2025-5551
Preprint. Discussion started: 5 December 2025

George, G., Stevens, B., Bony, S., Pincus, R., Fairall, C., Schulz, H., Kölling, T., Kalen, Q. T., Klingebiel, M., Konow, H., Lundry, A., Prange, M., and Radtke, J.: JOANNE: Joint dropsonde Observations of the Atmosphere in tropical North atlaNtic meso-scale Environments, Earth System Science Data, 13, 5253–5272, https://doi.org/10.5194/essd-13-5253-2021, publisher: Copernicus GmbH, 2021.

Grabowski, W. W., Dziekan, P., and Pawlowska, H.: Lagrangian condensation microphysics with Twomey CCN activation, Geoscientific Model Development, 11, 103–120, https://doi.org/10.5194/gmd-11-103-2018, 2018.

Hill, A. A., Lebo, Z. J., Andrejczuk, M., Arabas, S., Dziekan, P., Field, P., Gettelman, A., Hoffmann, F., Pawlowska, H., Onishi, R., and Vié, B.: Toward a Numerical Benchmark for Warm Rain Processes, Journal of the Atmospheric Sciences, 80, 1329–1359, https://doi.org/10.1175/JAS-D-21-0275.1, publisher: American Meteorological Society Section: Journal of the Atmospheric Sciences, 2023.

Hoffmann, F., Raasch, S., and Noh, Y.: Entrainment of aerosols and their activation in a shallow cumulus cloud studied with a coupled LCM–LES approach, Atmospheric Research, 156, 43–57, https://doi.org/10.1016/j.atmosres.2014.12.008, 2015.

Hu, Z. and Srivastava, R. C.: Evolution of Raindrop Size Distribution by Coalescence, Breakup, and Evaporation: Theory and Observations, Journal of the Atmospheric Sciences, 52, 1761–1783, https://doi.org/10.1175/1520-0469(1995)052<1761:EORSDB>2.0.CO;2, publisher: American Meteorological Society Section: Journal of the Atmospheric Sciences, 1995.

Igel, A. L. and Van Den Heever, S. C.: The Importance of the Shape of Cloud Droplet Size Distributions in Shallow Cumulus Clouds. Part II: Bulk Microphysics Simulations, Journal of the Atmospheric Sciences, 74, 259–273, https://doi.org/10.1175/jas-d-15-0383.1, publisher: American Meteorological Society, 2017a.

Igel, A. L. and Van Den Heever, S. C.: The Importance of the Shape of Cloud Droplet Size Distributions in Shallow Cumulus Clouds. Part I: Bin Microphysics Simulations, Journal of the Atmospheric Sciences, 74, 249–258, https://doi.org/10.1175/jas-d-15-0382.1, publisher: American Meteorological Society, 2017b.

Köhler, H.: The nucleus in and the growth of hygroscopic droplets, Transactions of the Faraday Society, 32, 1152–1161, https://doi.org/10.1039/TF9363201152, publisher: The Royal Society of Chemistry, 1936.

Langmuir., I.: The Evaporation of Small Spheres, Physical Review, 12, 368–370, https://doi.org/10.1103/physrev.12.368, publisher: American Physical Society (APS), 1918.

Leandro, M. and Chuang, P.: ATOMIC aircraft microphysics: Size-resolved cloud and aerosol number concentrations taken from N43 aircraft in the North Atlantic Ocean, Barbados: Atlantic Tradewind Ocean-Atmosphere Mesoscale Interaction Campaign 2020-01-31 to 2020-02-10 (NCEI Accession 0232458), https://doi.org/10.25921/VWVQ-5015, 2021.

Long, A. B.: Solutions to the Droplet Collection Equation for Polynomial Kernels, Journal of the Atmospheric Sciences, 31, 1040–1052, https://doi.org/10.1175/1520-0469(1974)031<1040:STTDCE>2.0.CO;2, publisher: American Meteorological Society Section: Journal of the Atmospheric Sciences, 1974.

Morrison, H., van Lier-Walqui, M., Fridlind, A. M., Grabowski, W. W., Harrington, J. Y., Hoose, C., Korolev, A., Kumjian, M. R., Milbrandt, J. A., Pawlowska, H., Posselt, D. J., Prat, O. P., Reimel, K. J., Shima, S.-I., van Diedenhoven, B., and Xue, L.: Confronting the Challenge of Modeling Cloud and Precipitation Microphysics, Journal of Advances in Modeling Earth Systems, 12, e2019MS001 689, https://doi.org/10.1029/2019MS001689, _eprint: https://onlinelibrary.wiley.com/doi/pdf/10.1029/2019MS001689, 2020.

Morrison, H., Chandrakar, K. K., Shima, S.-I., Dziekan, P., and Grabowski, W. W.: Impacts of Stochastic Coalescence Variability on Warm Rain Initiation Using Lagrangian Microphysics in Box and Large-Eddy Simulations, Journal of the Atmospheric Sciences, 81, 1067–1093, https://doi.org/10.1175/JAS-D-23-0132.1, publisher: American Meteorological Society Section: Journal of the Atmospheric Sciences, 2024.

Narenpitak, P., Kazil, J., Yamaguchi, T., Quinn, P., and Feingold, G.: From Sugar to Flowers: A Transition of Shallow Cumulus Organization During ATOMIC, Journal of Advances in Modeling Earth Systems, 13, e2021MS002 619, https://doi.org/10.1029/2021MS002619, 2021.

https://doi.org/10.5194/egusphere-2025-5551
Preprint. Discussion started: 5 December 2025

Naumann, A. K. and Seifert, A.: A Lagrangian drop model to study warm rain microphysical processes in shallow cumulus, Journal of Advances in Modeling Earth Systems, 7, 1136–1154, https://doi.org/10.1002/2015MS000456, 2015.

Naumann, A. K. and Seifert, A.: Recirculation and growth of raindrops in simulated shallow cumulus, Journal of Advances in Modeling Earth Systems, 8, 520–537, https://doi.org/10.1002/2016MS000631, 2016.

Nuijens, L., Stevens, B., and Siebesma, A. P.: The Environment of Precipitating Shallow Cumulus Convection, Journal of the Atmospheric Sciences, 66, 1962–1979, https://doi.org/10.1175/2008JAS2841.1, publisher: American Meteorological Society Section: Journal of the Atmospheric Sciences, 2009.

Pincus, R., Fairall, C. W., Bailey, A., Chen, H., Chuang, P. Y., de Boer, G., Feingold, G., Henze, D., Kalen, Q. T., Kazil, J., Leandro, M., Lundry, A., Moran, K., Naeher, D. A., Noone, D., Patel, A. J., Pezoa, S., PopStefanija, I., Thompson, E. J., Warnecke, J., and Zuidema, P.: Observations from the NOAA P-3 aircraft during ATOMIC, Earth System Science Data, 13, 3281–3296, https://doi.org/10.5194/essd-13-3281-2021, publisher: Copernicus GmbH, 2021.

Pruppacher, H. and Klett, J.: Microphysics of Clouds and Precipitation, vol. 18 of *Atmospheric and Oceanographic Sciences Library*, Springer Netherlands, Dordrecht, ISBN 978-0-7923-4211-3 978-0-306-48100-0, https://doi.org/10.1007/978-0-306-48100-0, 2010.

Radtke, J., Naumann, A. K., Hagen, M., and Ament, F.: The relationship between precipitation and its spatial pattern in the trades observed during EUREC4A, Quarterly Journal of the Royal Meteorological Society, 148, 1913–1928, https://doi.org/10.1002/qj.4284, _eprint: https://rmets.onlinelibrary.wiley.com/doi/pdf/10.1002/qj.4284, 2022.

Radtke, J., Vogel, R., Ament, F., and Naumann, A. K.: Spatial Organisation Affects the Pathway to Precipitation in Simulated Trade-Wind Convection, Geophysical Research Letters, 50, e2023GL103 579, https://doi.org/10.1029/2023GL103579, _eprint: https://onlinelibrary.wiley.com/doi/pdf/10.1029/2023GL103579, 2023.

Riechelmann, T., Noh, Y., and Raasch, S.: A new method for large-eddy simulations of clouds with Lagrangian droplets including the effects of turbulent collision, New Journal of Physics, 14, 065 008, https://doi.org/10.1088/1367-2630/14/6/065008, publisher: IOP Publishing, 2012.

Rochetin, N., Hohenegger, C., Touzé-Peiffer, L., and Villefranque, N.: A Physically Based Definition of Convectively Generated Density Currents: Detection and Characterization in Convection-Permitting Simulations, Journal of Advances in Modeling Earth Systems, 13, e2020MS002 402, https://doi.org/10.1029/2020MS002402, _eprint: https://onlinelibrary.wiley.com/doi/pdf/10.1029/2020MS002402, 2021.

Rogers, R. R., Baumgardner, D., Ethier, S. A., Carter, D. A., and Ecklund, W. L.: Comparison of Raindrop Size Distributions Measured by Radar Wind Profiler and by Airplane, Journal of Applied Meteorology and Climatology, 32, 694–699, https://doi.org/10.1175/1520-0450(1993)032<0694:CORSDM>2.0.CO;2, publisher: American Meteorological Society Section: Journal of Applied Meteorology and Climatology, 1993.

Sarkar, M., Bailey, A., Blossey, P., De Szoeke, S. P., Noone, D., Quiñones Meléndez, E., Leandro, M. D., and Chuang, P. Y.: Sub-cloud rain evaporation in the North Atlantic winter trade winds derived by pairing isotopic data with a bin-resolved microphysical model, Atmospheric Chemistry and Physics, 23, 12 671–12 690, https://doi.org/10.5194/acp-23-12671-2023, 2023.

Sarkar, M., Vogel, R., and Zheng, Y.: Microphysics Dominates the Sub-Cloud Rain Evaporation in the North Atlantic Trades, https://doi.org/10.22541/essoar.173809960.04642324/v1, 2025.

Schlottke, J., Straub, W., Beheng, K. D., Gomaa, H., and Weigand, B.: Numerical Investigation of Collision-Induced Breakup of Raindrops. Part I: Methodology and Dependencies on Collision Energy and Eccentricity, Journal of the Atmospheric Sciences, 67, 557–575, https://doi.org/10.1175/2009JAS3174.1, 2010.

Schulz, H., Eastman, R. M., and Stevens, B.: Characterization and Evolution of Organized Shallow Convection in the Trades, https://doi.org/10.1002/essoar.10505836.1, 2021.

https://doi.org/10.5194/egusphere-2025-5551
Preprint. Discussion started: 5 December 2025

Seifert, A.: On the Parameterization of Evaporation of Raindrops as Simulated by a One-Dimensional Rainshaft Model, Journal of the Atmospheric Sciences, 65, 3608–3619, https://doi.org/10.1175/2008JAS2586.1, 2008.

Seifert, A. and Heus, T.: Large-eddy simulation of organized precipitating trade wind cumulus clouds, Atmospheric Chemistry and Physics, 13, 5631–5645, https://doi.org/10.5194/acp-13-5631-2013, 2013.

Shima, S., Kusano, K., Kawano, A., Sugiyama, T., and Kawahara, S.: The super-droplet method for the numerical simulation of clouds and precipitation: a particle-based and probabilistic microphysics model coupled with a non-hydrostatic model: SUPER-DROPLET METHOD FOR CLOUDS AND PRECIPITATION, Quarterly Journal of the Royal Meteorological Society, 135, 1307–1320, https://doi.org/10.1002/qj.441, 2009.

Simmel, M., Trautmann, T., and Tetzlaff, G.: Numerical solution of the stochastic collection equation—comparison of the Linear Discrete Method with other methods, Atmospheric Research, 61, 135–148, https://doi.org/10.1016/S0169-8095(01)00131-4, 2002.

Srivastava, R. C.: A Simple Model of Evaporatively Driven Dowadraft: Application to Microburst Downdraft, Journal of the Atmospheric Sciences, 42, 1004–1023, https://doi.org/10.1175/1520-0469(1985)042<1004:ASMOED>2.0.CO;2, publisher: American Meteorological Society Section: Journal of the Atmospheric Sciences, 1985.

Srivastava, R. C.: A Model of Intense Downdrafts Driven by the Melting and Evaporation of Precipitation, Journal of the Atmospheric Sciences, 44, 1752–1774, https://doi.org/10.1175/1520-0469(1987)044<1752:AMOIDD>2.0.CO;2, 1987.

Stevens, B., Farrell, D., Hirsch, L., Jansen, F., Nuijens, L., Serikov, I., Brügmann, B., Forde, M., Linne, H., Lonitz, K., and Prospero, J. M.: The Barbados Cloud Observatory: Anchoring Investigations of Clouds and Circulation on the Edge of the ITCZ, Bulletin of the American Meteorological Society, 97, 787–801, https://doi.org/10.1175/bams-d-14-00247.1, publisher: American Meteorological Society, 2016.

Stevens, B., Bony, S., Farrell, D., Ament, F., Blyth, A., Fairall, C., Karstensen, J., Quinn, P. K., Speich, S., Acquistapace, C., Aemisegger, F., Albright, A. L., Bellenger, H., Bodenschatz, E., Caesar, K.-A., Chewitt-Lucas, R., de Boer, G., Delanoë, J., Denby, L., Ewald, F., Fildier, B., Forde, M., George, G., Gross, S., Hagen, M., Hausold, A., Heywood, K. J., Hirsch, L., Jacob, M., Jansen, F., Kinne, S., Klocke, D., Kölling, T., Konow, H., Lothon, M., Mohr, W., Naumann, A. K., Nuijens, L., Olivier, L., Pincus, R., Pöhlker, M., Reverdin, G., Roberts, G., Schnitt, S., Schulz, H., Siebesma, A. P., Stephan, C. C., Sullivan, P., Touzé-Peiffer, L., Vial, J., Vogel, R., Zuidema, P., Alexander, N., Alves, L., Arixi, S., Asmath, H., Bagheri, G., Baier, K., Bailey, A., Baranowski, D., Baron, A., Barrau, S., Barrett, P. A., Batier, F., Behrendt, A., Bendinger, A., Beucher, F., Bigorre, S., Blades, E., Blossey, P., Bock, O., Böing, S., Bosser, P., Bourras, D., Bouruet-Aubertot, P., Bower, K., Branellec, P., Branger, H., Brennek, M., Brewer, A., Brilouet, P.-E., Brügmann, B., Buehler, S. A., Burke, E., Burton, R., Calmer, R., Canonici, J.-C., Carton, X., Cato Jr., G., Charles, J. A., Chazette, P., Chen, Y., Chilinski, M. T., Choularton, T., Chuang, P., Clarke, S., Coe, H., Cornet, C., Coutris, P., Couvreux, F., Crewell, S., Cronin, T., Cui, Z., Cuypers, Y., Daley, A., Damerell, G. M., Dauhut, T., Deneke, H., Desbios, J.-P., Dörner, S., Donner, S., Douet, V., Drushka, K., Dütsch, M., Ehrlich, A., Emanuel, K., Emmanouilidis, A., Etienne, J.-C., Etienne-Leblanc, S., Faure, G., Feingold, G., Ferrero, L., Fix, A., Flamant, C., Flatau, P. J., Foltz, G. R., Forster, L., Furtuna, I., Gadian, A., Galewsky, J., Gallagher, M., Gallimore, P., Gaston, C., Gentemann, C., Geyskens, N., Giez, A., Gollop, J., Gouirand, I., Gourbeyre, C., de Graaf, D., de Groot, G. E., Grosz, R., Güttler, J., Gutleben, M., Hall, K., Harris, G., Helfer, K. C., Henze, D., Herbert, C., Holanda, B., Ibanez-Landeta, A., Intrieri, J., Iyer, S., Julien, F., Kalesse, H., Kazil, J., Kellman, A., Kidane, A. T., Kirchner, U., Klingebiel, M., Körner, M., Kremper, L. A., Kretzschmar, J., Krüger, O., Kumala, W., Kurz, A., L'Hégaret, P., Labaste, M., Lachlan-Cope, T., Laing, A., Landschützer, P., Lang, T., Lange, D., Lange, I., Laplace, C., Lavik, G., Laxenaire, R., Le Bihan, C., Leandro, M., Lefevre, N., Lena, M., Lenschow, D., Li, Q., Lloyd, G., Los, S., Losi, N., Lovell, O., Luneau, C., Makuch, P., Malinowski, S., Manta, G., Marinou, E., Marsden, N., Masson, S., Maury, N., Mayer, B., Mayers-Als, M., Mazel, C., McGeary, W., McWilliams, J. C., Mech, M., Mehlmann, M., Meroni, A. N., Mieslinger, T., Minikin, A., Minnett, P., Möller, G., Morfa Avalos, Y., Muller, C., Musat, I., Napoli, A., Neuberger, A., Noisel, C., Noone, D., Nordsiek, F., Nowak, J. L., Oswald, L., Parker, D. J., Peck, C., Person, R., Philippi, M., Plueddemann, A., Pöhlker, C., Pörtge, V., Pöschl, U., Pologne, L., Posyniak, M., Prange, M., Quiñones Meléndez, E., Radtke,

https://doi.org/10.5194/egusphere-2025-5551
Preprint. Discussion started: 5 December 2025

J., Ramage, K., Reimann, J., Renault, L., Reus, K., Reyes, A., Ribbe, J., Ringel, M., Ritschel, M., Rocha, C. B., Rochetin, N., Röttenbacher, J., Rollo, C., Royer, H., Sadoulet, P., Saffin, L., Sandiford, S., Sandu, I., Schäfer, M., Schemann, V., Schirmacher, I., Schlenczek, O., Schmidt, J., Schröder, M., Schwarzenboeck, A., Sealy, A., Senff, C. J., Serikov, I., Shohan, S., Siddle, E., Smirnov, A., Späth, F., Spooner, B., Stolla, M. K., Szkółka, W., de Szoeke, S. P., Tarot, S., Tetoni, E., Thompson, E., Thomson, J., Tomassini, L., Totems, J., Ubele, A. A., Villiger, L., von Arx, J., Wagner, T., Walther, A., Webber, B., Wendisch, M., Whitehall, S., Wiltshire, A., Wing, A. A., Wirth, M., Wiskandt, J., Wolf, K., Worbes, L., Wright, E., Wulfmeyer, V., Young, S., Zhang, C., Zhang, D., Ziemen, F., Zinner, T., and Zöger, M.: EUREC^{4}A, Earth System Science Data, 13, 4067–4119, https://doi.org/10.5194/essd-13-4067-2021, publisher: Copernicus GmbH, 2021.

Straub, W., Beheng, K. D., Seifert, A., Schlottke, J., and Weigand, B.: Numerical Investigation of Collision-Induced Breakup of Raindrops. Part II: Parameterizations of Coalescence Efficiencies and Fragment Size Distributions, Journal of the Atmospheric Sciences, 67, 576–588, https://doi.org/10.1175/2009JAS3175.1, publisher: American Meteorological Society Section: Journal of the Atmospheric Sciences, 2010.

Sölch, I. and Kärcher, B.: A large-eddy model for cirrus clouds with explicit aerosol and ice microphysics and Lagrangian ice particle tracking, Quarterly Journal of the Royal Meteorological Society, 136, 2074–2093, https://doi.org/10.1002/qj.689, 2010.

Touzé-Peiffer, L., Vogel, R., and Rochetin, N.: Cold Pools Observed during EUREC4A: Detection and Characterization from Atmospheric Soundings, Journal of Applied Meteorology and Climatology, 61, 593–610, https://doi.org/10.1175/JAMC-D-21-0048.1, publisher: American Meteorological Society Section: Journal of Applied Meteorology and Climatology, 2022.

Tridon, F., Battaglia, A., and Watters, D.: Evaporation in action sensed by multiwavelength Doppler radars, Journal of Geophysical Research: Atmospheres, 122, 9379–9390, https://doi.org/10.1002/2016JD025998, _eprint: https://onlinelibrary.wiley.com/doi/pdf/10.1002/2016JD025998, 2017.

Unterstrasser, S., Hoffmann, F., and Lerch, M.: Collection/aggregation algorithms in Lagrangian cloud microphysical models: rigorous evaluation in box model simulations, Geoscientific Model Development, 10, 1521–1548, https://doi.org/10.5194/gmd-10-1521-2017, publisher: Copernicus GmbH, 2017.

Unterstrasser, S., Hoffmann, F., and Lerch, M.: Collisional growth in a particle-based cloud microphysical model: insights from column model simulations using LCM1D (v1.0), Geoscientific Model Development, 13, 5119–5145, https://doi.org/10.5194/gmd-13-5119-2020, publisher: Copernicus GmbH, 2020.

Vogel, R., Konow, H., Schulz, H., and Zuidema, P.: A climatology of trade-wind cumulus cold pools and their link to mesoscale cloud organization, Atmospheric Chemistry and Physics, 21, 16 609–16 630, https://doi.org/10.5194/acp-21-16609-2021, publisher: Copernicus GmbH, 2021.

Zuidema, P., Li, Z., Hill, R. J., Bariteau, L., Rilling, B., Fairall, C., Brewer, W. A., Albrecht, B., and Hare, J.: On Trade Wind Cumulus Cold Pools, Journal of the Atmospheric Sciences, 69, 258–280, https://doi.org/10.1175/JAS-D-11-0143.1, 2012.

Zuidema, P., Torri, G., Muller, C., and Chandra, A.: A Survey of Precipitation-Induced Atmospheric Cold Pools over Oceans and Their Interactions with the Larger-Scale Environment, in: Shallow Clouds, Water Vapor, Circulation, and Climate Sensitivity, edited by Pincus, R., Winker, D., Bony, S., and Stevens, B., pp. 111–133, Springer International Publishing, Cham, ISBN 978-3-319-77273-8, https://doi.org/10.1007/978-3-319-77273-8_6, 2017.